5-2009

Imaging Second-Harmonic Radiation and Scattering Patterns in ZnO Micro/Nanostructures

Katrina Marie Geren
University of Arkansas, Fayetteville

Recommended Citation

Geren, Katrina Marie, "Imaging Second-Harmonic Radiation and Scattering Patterns in ZnO Micro/Nanostructures" (2009). *Theses and Dissertations*. 43.
http://scholarworks.uark.edu/etd/43

Imaging Second-Harmonic Radiation and Scattering Patterns in ZnO Micro/Nanostructures

Imaging Second-Harmonic Radiation and Scattering Patterns in ZnO Micro/Nanostructures

A thesis submitted in partial fulfillment
of the requirements for the degree of
Master of Science in Microelectronics-Photonics

By

Katrina Geren
Oklahoma State University
Bachelor of Science in Electrical Engineering, 2006

May 2009
University of Arkansas

Abstract

The optical characteristics of ZnO nanostructures have recently garnered interest due to the inclusion of these structures in many nanoscale optical and optoelectronic devices. This thesis will address several characteristics involving second harmonic generation and scattering in ZnO nano- and microstructures. A method will be presented for determining the nonlinear coefficients of the second order susceptibility in a single ZnO rod. This method uses transmission geometry where previous methods have employed back-reflected irradiation. The nonlinear coefficients found using this new technique were consistent with previous data from similar structures.

Models will be presented for predicting the second harmonic scattering patterns from both ZnO tetrapods and joined rods. The models are based on infinitely thin finite dipoles. The model for two joined rods showed good agreement with experimental data, while the model for the tetrapod showed only minor agreement.

This thesis is approved for
recommendation to the
Graduate Council

Thesis Director:

Dr. Min Xiao

Thesis Committee:

Dr. Hameed Naseem

Dr. Z. Ryan Tian

Professor Ken Vickers

Thesis Duplication Release

I hereby authorize the University of Arkansas Libraries to duplicate this thesis when needed for research and/or scholarship.

Agreed________________________________
Katrina Geren

Refused________________________________
Katrina Geren

Acknowledgements

I would like to thank Dr. Tian and Dr. Huajun Zhou for providing sample structures for the work in this thesis. I would also like to thank Renee Hearon for making sure that I actually got together everything that I was supposed to in order to graduate. Finally, I need to thank Rob Sleezer for giving me excellent programming advice.

This program is financially supported by the National Science Foundation under S-STEM Grant No. DUE-0728636. Any opinions, findings, and conclusions or recommendations expressed in this material are those of the author and do not necessarily reflect the views of the National Science Foundation.

Table of Contents

Abstract ii

Thesis Duplication Release iv

Acknowledgements v

List of Figures viii

Chapter 1: Introduction 1

- 1.1 Properties of Zinc Oxide 1
- 1.2 Second Harmonic Generation 3
- 1.3 Second Harmonic Generation in ZnO and Nanorods 5

Chapter 2: Determining the Nonlinear Coefficients for ZnO Rods 7

- 2.1 Explanation of Nonlinear Coefficients 7
- 2.2 Previous Work 7
- 2.3 Experimental Setup 8
- 2.4 Mathematical Formulation 10
- 2.5 Results 14

Chapter 3: Imaging Second Harmonic Radiation in ZnO Rods 18

Chapter 4: Radiation Patterns of More Complex Structures 25

- 4.1 Two Joined Rods 25
- 4.2 Tetrapod 36

Chapter 5: Other Experimental Results 43

- 5.1 Propagation of Light Through Structures 43
- 5.2 Photoluminescence 47

Chapter 6: Conclusions 50

References 51

Appendix A: Matlab code used to simulate the a single dipole......................................53

Appendix B: Matlab code used to simulate the three-dimensional twinned tetrapod structure...56

Appendix C: Description of Research for Popular Publication 60

Appendix D: Executive Summary of Newly Created Intellectual Property 64

Appendix E: Potential Patent and Commercialization Aspects of listed Intellectual Property Items 65

  E.1 Patentability of Intellectual Property 65

  E.2 Commercialization Prospects 65

  E.3 Possible Prior Disclosure of IP 66

Appendix F: Broader Impact of Research 67

  F.1 Applicability of Research Methods to Other Problems 67

  F.2 Impact of Research Results on U.S. and Global Society 67

  F.3 Impact of Research Results on the Environment 67

Appendix G: Microsoft Project for MS MicroEP Degree Plan 68

Appendix H: Identification of All Software Used in Research and Thesis Generation 71

List of Figures

Figure 1: Top view of the experimental setup on an optical table for determining nonlinear coefficients from Geren et al.[21] 9

Figure 2: Assumed geometry for determination of nonlinear coefficients from Geren et al. [21] 11

Figure 3: Polarization diagrams for a sample ZnO rod from Geren et al.[21] 15

Figure 4: Coordinate system of the dipole simulations. 19

Figure 5: Top view of the experimental layout on an optical table for acquiring second harmonic scattering images 20

Figure 6: Flow chart of dipole simulation program. 22

Figure 7: Simulated image of the dipole Poynting vector (A), experimental image of second harmonic scatter from Liu et al (B), and simulated image of the dipole Poynting vector from Liu et al (C).[20] 23

Figure 8: Vector simulation of a dipole rod in: original resolution (A) and adjusted resolution (B). 24

Figure 9: Typical Example of tetrapod samples. 25

Figure 10: Planar model of two joined rods 26

Figure 11: Simulation of two joined dipoles 27

Figure 12: Experimental second harmonic scattering pattern for two joined rods. 28

Figure 13: Simulation results for two joined rods with the dipole moment directed perpendicular to the length of the rod. 29

Figure 14: Assumed geometric orientation of the joined rod model. 30

Figure 15: Comparison between the experimental image (A) and the 3D simulation results (B) for two joined rods. 33

Figure 16: Setup of twinned model of two joined rods. 34

Figure 17: Results from three dimensional simulation of two twinned joined dipoles. .. 35

Figure 18: Planar Y-formation model. 36

Figure 19: Two dimensional tetrapod simulation (A) compared with experimental tetrapod second harmonic pattern (B). 38

Figure 20: Tetrapod model. 39

Figure 21: Experimental second order scatter patterns from a 7.9 µm tetrapod (A) and a 13.8 µm tetrapod (B). 40

Figure 22: Three dimensional simulation of 13.8 µm tetrapod. 41

Figure 23: Three dimensional simulation of twinned dipoles with a length of 8 µm. 42

Figure 24: Experimental setup for investigating propagation. 44

Figure 25: Excitation (A) and scatter (B) from a partial tetrapod. 46

Figure 26: Photoluminescence from the vertical leg of a tetrapod. 48

Figure 27: Photoluminescence from the horizontal leg of a partial tetrapod. 49

Chapter 1: Introduction

1.1 Properties of Zinc Oxide

Recently the material zinc oxide has garnered increasing interest due to its many favorable qualities that make it a good choice for a multitude of situations. It is biosafe and chemically stable which makes it useful in situations when more volatile materials would not be practical.[1,2] It is also environmentally friendly which is becoming increasingly important.[2] Its piezoelectric and pyroelectric properties make it useful for many different applications while the availability of high quality bulk crystals makes it practical.[1,3] Recent focus has been on its uses in optoelectronic devices. Its wide bandgap and large exiton binding energy make it a good candidate for room temperature optical devices.[1,2,3] Specifically, it is a good choice for a room temperature ultraviolet emitter. While the ultraviolet radiation stems from exiton emissions, photoluminescence from defects in many colors, primarily blue and green has also been reported.[3] Another favorable quality that makes it useful in many transistor applications is that it is a transparent conductor.[1] What really makes ZnO an interesting material is the many different types of nanostructures that can be synthesized under specific conditions. Nanorods, wires, tetrapods, needles, springs, and combs have all been reported.[1] Though the photoluminescence spectra of these structures vary, they all have useful properties and have already been used to fabricate many different devices.[2]

One of the most fundamental devices that has been created from ZnO nanostructures is the light emitting diode reported by Konekamp et al. in 2004.[4] They created an LED from vertically oriented nanowires that emitted across the entire visible spectrum due to the defect emissions mentioned above and produced white light.

ZnO nanowires and disks have also been credited with waveguiding capabilities. Nanowires have been reported to behave very similarly to circular step index optical fibers.[5,6] They guide both transverse electric and transverse magnetic modes and have been shown to carry both single and multimode operation. Waveguide activity in disks has mostly been seen in the whispering gallery modes.[7] In this case light is directed around the inner edge of the structure boundary by total internal reflection.

The most popular optical research is currently focused on the lasing capabilities of ZnO nanostructures. Lasing has been reported in nanowires, rods, ribbons, tetrapods, and combs.[2,8,9,10,11,12] There are two different gain mechanisms reported for this lasing activity, exiton-exiton scattering and electron-hole plasma recombination.[2] The exiton-exiton mechanism is the more interesting as the lasing threshold for this mechanism is 2-3 times smaller than that of the electron-hole plasma recombination. There are also two different types of feedback mechanisms reported for this behavior. Scientists have reported both the use of Fabry-Perot resonators as the laser feedback mechanisms and multiple scattering events which result in random lasing.[2] Lasing from the exiton-exiton emissions has been reported even at room temperature. At this point no lasing has been reported from electrical pumping; all reported cases have relied upon optical pumping.

The property most relevant to this work is the lack of central symmetry in the crystal that leads to the material's nonzero second order susceptibility. This is the property that leads to the second-harmonic radiation that is the primary interest of this work. Recently, this property has led to the use of ZnO nanocrystals as optical bioprobes.

One study incorporated the ZnO nanocrystals with Folic Acid molecules to target and image tumor cells. [13]

1.2 Second Harmonic Generation

As mentioned above, second harmonic generation is a function of a material's second order susceptibility. A material's susceptibility is a measure of how easily it can be polarized in an applied electric field. Due to the complex structure of the materials, this is actually a tensor value that describes how easily the material is polarized in each individual direction.

Second harmonic generation occurs when an incident field causes a material to polarize with a quadratic dependence upon that incident field amplitude. This polarization then acts as the source term in Maxwell's equations for a field having twice the frequency of the original field incident upon the structure. The simplified mathematical formulation of this is as follows:[14] If the electric field is assumed to be of the form

$$E_j^{\omega}(t) = \frac{1}{2}\left(E_{0j}^{\omega} e^{i\omega t} + c.c\right), \qquad \text{(Equation 1)}$$

and the polarization is defined as

$$P_i = \varepsilon_0 \chi_{ij} E_j + 2d_{ijk} E_j E_k + 4\chi_{ijkl} E_j E_k E_l + \ldots \qquad \text{(Equation 2)}$$

then the second order portion of the polarization is

$$P_i(t) = 2d_{ijk}\,\frac{1}{2}\left(E_{0j}^{\omega} e^{i\omega t} + E_{0j}^{\omega} e^{i\omega t} + c.c\right) \times \left(E_{0k}^{\omega} e^{i\omega t} + E_{0k}^{\omega} e^{i\omega t} + c.c\right). \qquad \text{(Equation 3)}$$

In these equations, ijkl indicate positive integers, ω is the frequency of the fundamental beam, χ is a susceptibility tensor, and d_{ijk} is $\frac{1}{2}\chi_{ijk}$. The element of this polarization relating to the second harmonic (SH) follows the form

$$P_i^{2\omega}(t)=\frac{1}{2}P_{0i}^{2\omega}e^{i2\omega t}+c.c.=d_{ijk}\left(\frac{1}{2}E_{0j}^{\omega}e^{i\omega t}+c.c.\right)\times\left(\frac{1}{2}E_{0k}^{\omega}e^{i\omega t}+c.c.\right). \qquad \text{(Equation 4)}$$

When looking just at the magnitudes in this equation, the quadratic dependence of the polarization becomes obvious,

$$P_{oi}^{2\omega}=d_{ijk}E_{0j}^{\omega}E_{0k}^{\omega}. \qquad \text{(Equation 5)}$$

When a crystal or material is centrosymmetric (has a center of inversion) the second order susceptibility cancels out and there is no second harmonic generation. Noncentrosymmetric materials such as ZnO are therefore needed, though small amounts of second harmonic radiation can actually be produced from the surface defects of centrosymmetric crystals. By nature they cannot be exactly symmetric at the edges of the structure and at these points, second harmonic radiation can be generated.

Second harmonic generation has many uses. It can yield information about a crystal's quality and structure or it can be used to double the frequency of a laser. It can also be used for imaging both thin films and biological structures. Second harmonic microscopy, an imaging technique that uses a laser scanning microscope to look at the second harmonic patterns from a material, has been used in several biomedical areas. It has been used to look at noncentrosymmetric structures such as collagen and microtubules.[15] For structures that are more symmetrical in nature, probes created from strongly noncentrosmmetric materials such as ZnO must be used for imaging. Recent studies have shown the feasibility of ZnO nanocrystals for the creation of these probes for imaging tumor cells.[13]

1.3 Second Harmonic Generation in ZnO and Nanorods

There is a growing body of research into the phenomenon of Second Harmonic Generation (SHG) in nanorods. Some researchers have concentrated on the scattering of the second harmonic radiation. Dadap recently published a paper detailing the mathematical implications of the scattering of second harmonic radiation from perfect cylinders of both centrosymmetric and noncentrosymmetric materials.[16] This work shows a direct correlation between the second harmonic scatter and the length and diameter of the cylinders. The equations were developed using the Raleigh-Gans-Debye approximation for plane wave excitation and assuming the cylinders were immersed in a perfectly or almost perfectly matched medium.

Near field scanning optical microscopy (NSOM) was used by one group at the University of California to determine the absolute magnitude of the two independent elements of the second order susceptibility tensor $\boldsymbol{\chi}^{(2)}$ in ZnO nanowires when Kleinman's symmetry is assumed.[17] A more recent paper dealing with ZnO thin films indicated that at a wavelength around 400 nm, Kleinman's symmetry does not apply and there are three independent elements to the $\boldsymbol{\chi}^{(2)}$ tensor.[18]

Reflected second harmonic radiation from GaN nanowires was investigated by Long et al.[19] They found that from the second harmonic radiation the crystallographic orientation of the wires could be distinguished. They found that if the nanowire cross section is small enough, the SH radiation can be approximated as dipole radiation driven by the second order polarization.

This leads fairly well into the previous work most pertinent to this thesis. Liu et al. reported a comparison between a dipole model and the second harmonic radiation patterns from ZnO nanorods.[20] This paper will examine the planar second harmonic radiation patterns from forward scatter versus dipole models of the same orientation. It will also investigate the affect of a twinning defect (when the polarity of the crystal changes in the middle of the rod at a ‘twinning plane’) on the second harmonic intensity pattern of the rod. In addition the relation demonstrated between the length of the nanorod and the number of fringing fields in its second harmonic pattern will be considered.

The primary motivation for this thesis is the extension of the above work as there are a number of potential applications for second harmonic radiation from nanostructures. It could be used in photodetectors, optical frequency doublers, probes for biomedical imaging, or simply as a convenient predictor of crystal structure.

Chapter 2: Determining the Nonlinear Coefficients for ZnO Rods

2.1 Explanation of Nonlinear Coefficients

A method for determining the nonlinear coefficients of the second order susceptibility tensor will be presented in this chapter. These coefficients determine the efficiencies of nonlinear optical processes such as frequency doubling. Here the coefficient for the second order susceptibility tensor will be found. This work has been accepted to be published in the *Journal of Applied Physics*.[21]

2.2 Previous Work

Previously the second order susceptibility tensors have been determined using both near field scanning microscopy (NSOM) and epi-fluorescence second order microscopy.[17,19] Both of these methods use back reflected irradiation and have many drawbacks. Back reflected irradiation is much weaker than forward irradiation and has a coherence length that is shorter than that of the forward irradiation by an order of magnitude, which leads to less accuracy in measurements. The shorter coherence length also conflicts with some of the assumptions for both of these methods at a second harmonic wavelength of 405 nm with structures on the order of 100 nm in width. Both methods assume that the coherence length of the back irradiation is much longer than the width of the structures, but in this case the coherence length would be roughly 49 nm which is actually shorter. Neither method is ideal for working with structures whose dimensions are on the same order of magnitude as the wavelengths used for analysis, which is unfortunate when one wants to look at nanostructures in the visible spectrum.

As mentioned above, back irradiation is quite weak when compared to forward irradiation, thus making forward irradiation a more desirable geometry to work in. The coherence length of the forward irradiation also has a much longer coherence length, allowing for more accurate measurement over an almost 10x greater distance.

2.3 Experimental Setup

The method that will be presented here relies on the polarization diagrams from transmitted forward irradiation.

The ZnO rods used in the study were several micrometers long and 100-250 nm in diameter. They were grown on a fused quartz substrate by the aqueous solution method and oriented parallel to the substrate.[22] The density of the rods was low enough that it was possible to view just one rod at a time. The samples were prepared by Dr. Huajun Zhou in the laboratory of Dr. Ryan Tian at the University of Arkansas.

A single sample rod was excited using a one watt mode-locked Ti:Sapphire laser (repetition rate of 82 MHz and temporal width of ~100 fs) at a wavelength of 810 nm focused to a spot size of roughly 100 μm, making the peak intensity on the sample about 40 MW/cm^2. The polarization of the incident beam was adjusted using a half-wave plate before the sample. A lens (L1; Φ=1 in, f=20 cm) and a long pass filter (LF) passing 750-2200 nm, were placed before the sample to focus the beam and filter out any incident second harmonic. A bandpass filter (BF) with a range of 350-650 nm after the sample selected the second harmonic radiation which was passed through an iris diaphragm (IR) and another lens (L2; Φ=1 in, f=20 cm), to focus the radiation as seen in Figure 1.

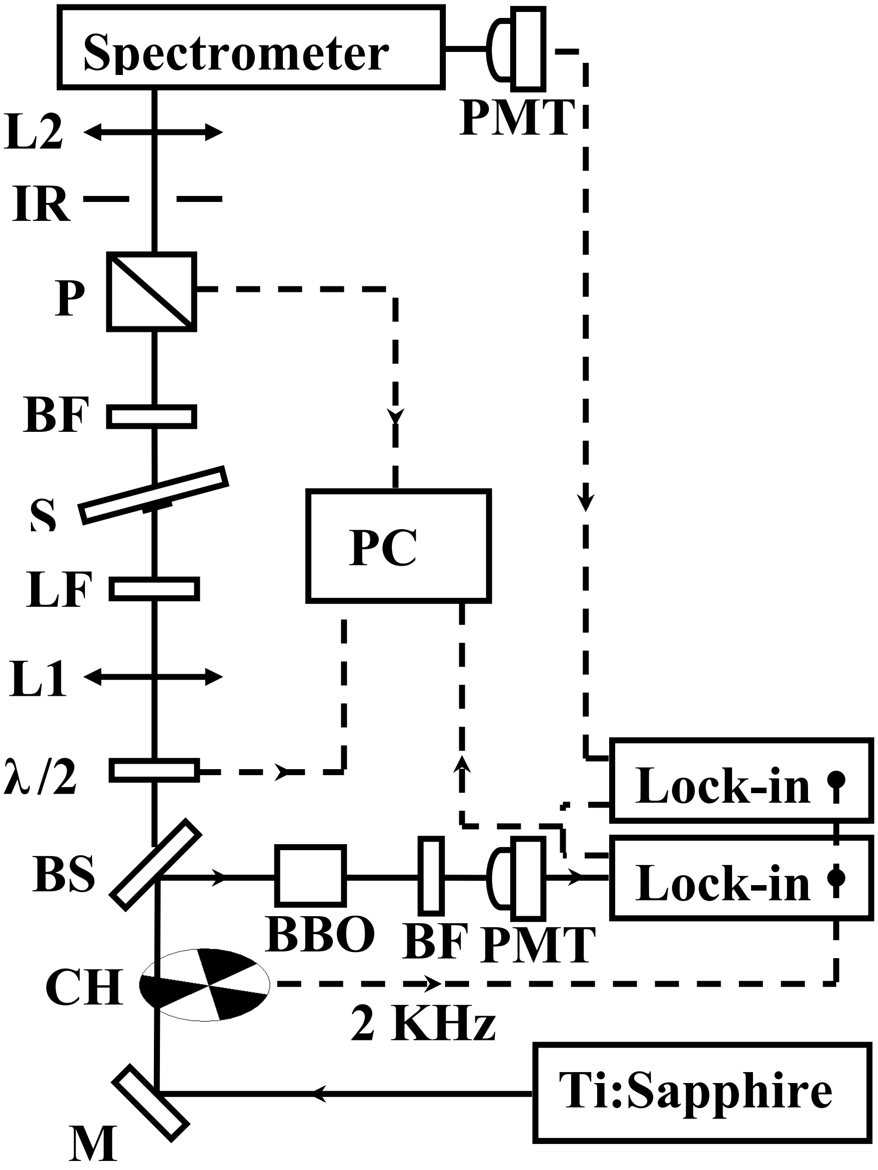

Figure 1: Top view of the experimental setup on an optical table for determining nonlinear coefficients from Geren et al.[21]

The iris diaphragm was used to eliminate the scatter and select only the coherent second harmonic radiation transmitted through the rod. The radiation was focused into a 0.5 m spectrometer and detected by a photomultiplier tube (PMT). A chopper (CH) and lock-in amplifier set at a frequency of 2 kHz were used to raise the signal to noise ratio.

Ten percent of the fundamental beam was redirected via a beam splitter (BS) through a nonlinear BBO crystal (β-BaB_2O_4) and was detected by a second PMT to act as a reference for fluctuations in the laser intensity. A single ZnO rod was originally located using a 50x objective and a Sony digital video camera.

2.4 Mathematical Formulation

Despite the simplification of the system allowed by the forward geometry, several assumptions were necessary in order to determine the nonlinear coefficients. First, the incident light was represented as a plane wave. This was allowable because the beam was only slightly focused. Also, the back irradiation reflected from the fused quartz substrate was neglected. Previous studies using this type of substrate have shown that this back irradiation is only 4% of the intensity of the light.[20] The coherence length of the back irradiation was an order of magnitude smaller than the forward irradiation as well. Because the scatter from the rod was essentially eliminated by the iris diaphragm it was also neglected.

Because of the assumptions made, the sample was able to be represented as the simple four layer system seen in Figure 2 consisting of: 1-Vacuum (Vac), 2-fused quartz (FQ), 3-ZnO (NR), and 4-vacuum. Since the scatter was neglected, this system could be treated using a thin film formula for the transmitted fields following the equations of Sipe et al.[23,24]

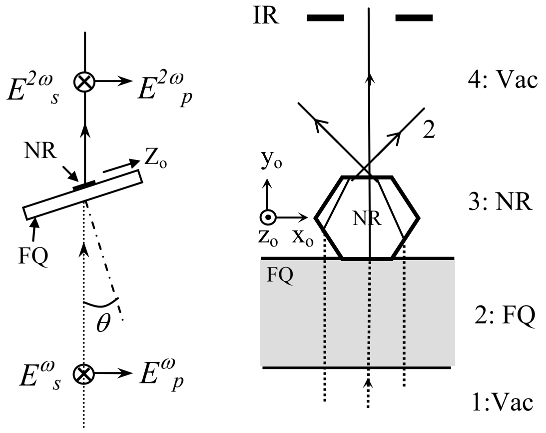

Figure 2: Assumed geometry for determination of nonlinear coefficients from Geren et al. [21]

The nonlinear polarization excited by the fundamental beam for the given geometry follows the form

$$\mathbf{P}^{2\omega}=\begin{pmatrix}P_s^{2\omega}\\ P_k^{2\omega}\\ P_z^{2\omega}\end{pmatrix}=\left[d'_{ij}\right]\times\begin{pmatrix}\left(t_\omega^s\right)^2\left(E_s^\omega\right)^2\\ \left(f_c t_\omega^p\right)^2\left(E_p^\omega\right)^2\\ \left(f_s t_\omega^p\right)^2\left(E_p^\omega\right)^2\\ 2f_s f_c\left(t_\omega^p\right)^2\left(E_p^\omega\right)^2\\ 2f_s t_\omega^s t_\omega^p E_s^\omega E_p^\omega\\ 2f_c t_\omega^s t_\omega^p E_s^\omega E_p^\omega\end{pmatrix}, \qquad \text{(Equation 6)}$$

where $t_\omega^{(s,p)}$ represents the Fresnel coefficients as

$$t_\omega^{(s,p)}=t_{12,\omega}^{(s,p)}T_{23,\omega}^{(s,p)},\ T_{23,\omega}^{(s,p)}=t_{23,\omega}^{(s,p)}/\left(1-r_{34,\omega}^{(s,p)}r_{32,\omega}^{(s,p)}e^{2iDw}\right). \qquad \text{(Equation 7a)}$$

The factors $r_{ij,\omega}^{(s,p)}$ and $t_{ij,\omega}^{(s,p)}$ represent the Fresnel reflection and transmission coefficients respectively from layer i to layer j. $T_{23,\omega}^{(s,p)}$ accounts for the internal reflection of the fundamental frequency inside the rod. The other values in the equation are defined as follows

$$f_s=\sin\theta/n_3,\ f_c=\sqrt{1-f_s^2}\ , \qquad \text{(Equation 7b)}$$

$$E_s^\omega = E^\omega \cos\varphi , \qquad \text{(Equation 7c)}$$

with φ defined as the incident polarization angle of the fundamental beam, (s=0, p=π/2). $\lfloor d'_{ij} \rfloor$ is the matrix form of the nonlinear susceptibility tensor χ_{ijk} of the 6mm symmetry class defined according to the orthogonal coordinate system ($\hat{\mathbf{s}}, \hat{\mathbf{k}}, \hat{\mathbf{z}}$) referenced to the incident beam. The plane of incidence for the excitation beam is defined as ($\hat{\boldsymbol{k}}, \hat{z}$). $\lfloor d'_{ij} \rfloor$ is defined as

$$\lfloor d'_{ij} \rfloor = \begin{bmatrix} 0 & 0 & 0 & 0 & 0 & d_{15} \\ d_{31} & d_{33} & d_{31} & 0 & 0 & 0 \\ 0 & 0 & 0 & d_{15} & 0 & 0 \end{bmatrix}, \qquad \text{(Equation 8)}$$

where each d_{ij} is a component of the standard susceptibility tensor defined according to the crystallographic coordinate axis. The matrix $\lfloor d'_{ij} \rfloor$ can be found from the crystallographic axis representation, $\lfloor d_{ij} \rfloor$, via the transformation $\chi'_{ijk} = \alpha_{il}\alpha_{jm}\alpha_{kn}\chi_{lmn}$, where $\lfloor \alpha_{ij} \rfloor$ is the coordinate matrix transform between each of the corresponding axis. Substituting this matrix into the polarization equation gives

$$\mathbf{P}^{2\omega} = \begin{pmatrix} P_s^{2\omega} \\ P_k^{2\omega} \\ P_z^{2\omega} \end{pmatrix} = \begin{bmatrix} 2d_{15} 2 f_c t_\omega^s t_\omega^p E_s^\omega E_p^\omega \\ d_{31}\left(\left(t_\omega^s\right)^2\left(E_s^\omega\right)^2 + \left(f_s t_\omega^p\right)^2\left(E_p^\omega\right)^2\right) + d_{33}\left(f_c t_\omega^p\right)^2\left(E_p^\omega\right)^2 \\ 2d_{15} 2 f_s f_c \left(t_\omega^p\right)^2\left(E_p^\omega\right)^2 \end{bmatrix} \qquad \text{(Equation 9)}$$

Following Sipe et al.,[23,24] the components of the transmitted second harmonic field after the sample are given by

$$E_s^{2\omega} = \frac{8\pi\omega^2}{c^2} iW^{-1} T_{34}^s \exp[iDW] \int_{-D}^{0} \exp[iz'W]\, \hat{\mathbf{s}} \cdot \mathbf{P}^{2\omega} \exp[-2iwz']dz' \qquad \text{(Equation 10a)}$$

$$E_P^{2\omega} = \frac{8\pi\omega^2}{c^2} iW^{-1} T_{34}^P \exp[iDW] \int_{-D}^{0} \exp[iz'W]\, \hat{\mathbf{P}}_- \cdot \mathbf{P}^{2\omega} \exp[-2iwz']dz' . \qquad \text{(Equation 10b)}$$

The variables are defined as follows:

$$T_{34,2\omega}^{(s,p)} = t_{34,2\omega}^{(s,p)} / \left(1 - r_{34,2\omega}^{(s,p)} r_{32,2\omega}^{(s,p)} e^{2iDW}\right),$$ (Equation 11a)

$$W = 2\omega / c\left(N_3^2 - \sin^2\theta\right)^{1/2}, w = \omega / c\left(n_3^2 - \sin^2\theta\right)^{1/2},$$ (Equation 11b)

$$\hat{\mathbf{P}}_{-} = F_s\hat{\mathbf{z}} + F_c\hat{\mathbf{k}},$$ (Equation 11c)

$$F_s = \sin\theta / N_3,\ F_c = \sqrt{1 - F_s^2}\ .$$ (Equation 11d)

In these equations, $\hat{\mathbf{s}}, \hat{\mathbf{k}}, \hat{\mathbf{z}}$ represent the unit vectors of the orthogonal coordinate system with θ defined as the angle of incidence of the fundamental beam. The coefficients $r_{ij,2\omega}^{(s,p)}$ and $t_{ij,2\omega}^{(s,p)}$ are the Fresnel reflection and transmission coefficients for the second harmonic radiation from layer i to layer j. The other Fresnel coefficient, $T_{34,2\omega}^{(s,p)}$, accounts for the internal reflectance of the rod. The refractive indices for each layer i are represented by N_i for the fundamental frequency (ω) and n_i for the second harmonic frequency (2ω). D represents the diameter of the ZnO rod.

If the ealier polarization equations are substituted into these equations for the second harmonic field, the complex amplitudes are found to be

$$E_s^{2\omega} = S_s\left(-2d_{15}f_c t_\omega^s t_\omega^p \cos\varphi\sin\varphi\right)\left(E^\omega\right)^2\ ,$$ (Equation 12a)

(Equation 12b)

$$E_p^{2\omega} = S_p\left[\left(2d_{15}f_c f_s F_s + d_{31}f_s^2 F_c + d_{33}f_c^2 F_c\right)\left(t_\omega^p\right)^2\cos^2\varphi + d_{31}F_c\left(t_\omega^s\right)^2\sin^2\varphi\right]\left(E^\omega\right)^2.$$

The variables are defined as follows

$$S_{(s,p)} = 8\omega^2 / c^2 W^{-1} T_{34,2\omega}^{(s,p)} e^{iDW}\left[1 - \exp\left(-i\pi D / L_{eff}\right)\right] L_{eff}\ ,$$ (Equation 13a)

$$L_{eff} = \pi\left(W - 2w\right)^{-1},$$ (Equation 13b)

with the variable L_{eff} representing the coherence length in the forward geometry. From these equations the transmitted second harmonic intensities can be fitted to the equations

$$I_s^{2\omega} = \left(c_s \cos\varphi \sin\varphi\right)^2, \qquad \text{(Equation 14a)}$$

$$I_p^{2\omega} = \left(a_p \cos^2\varphi + b_p \sin^2\varphi\right)^2, \qquad \text{(Equation 14b)}$$

with c_s, a_p, and b_p as the fitting parameters. Setting the coefficients of the cosine and sine elements in Equations (14b) and (12b) equal to each other, the following linear equation relating the coefficients of $\lfloor d'_{ij} \rfloor$ with the parameters a_p and b_p can be derived:

$$\left(\frac{d_{33}}{d_{31}}\right) + 2\frac{f_s F_s}{f_c F_c}\left(\frac{d_{15}}{d_{31}}\right) = \frac{t_s^2}{f_c^2 t_p^2}\left(\frac{a_p}{b_p}\right) - \frac{f_s^2}{f_c^2}. \qquad \text{(Equation 15)}$$

Since all of the elements of equation (10) other than the ratios of the elements of $\lfloor d'_{ij} \rfloor$ depend upon the incident angle of the fundamental beam, measurements were taken from two different incidence angles. Values for both sets of measurements were input into Equation (15) and the two versions were compared to acquire the ratios d_{33}/d_{31} and d_{15}/d_{31}.

2.5 Results

Both the p- and s-polarized second harmonic intensity from a sample rod as a function of fundamental beam polarization were measured at the incident angles of 90° and 27 ° as seen in Figure 3. As can be seen in Figure 3(B) the strongest second harmonic signal was the p-polarized output from a p-polarized incident beam shown on the 0° point. The theoretical fit lines in Figure 3 correspond to Equation (14) fit to the data using the fitting parameters c_s, a_p, and b_p.

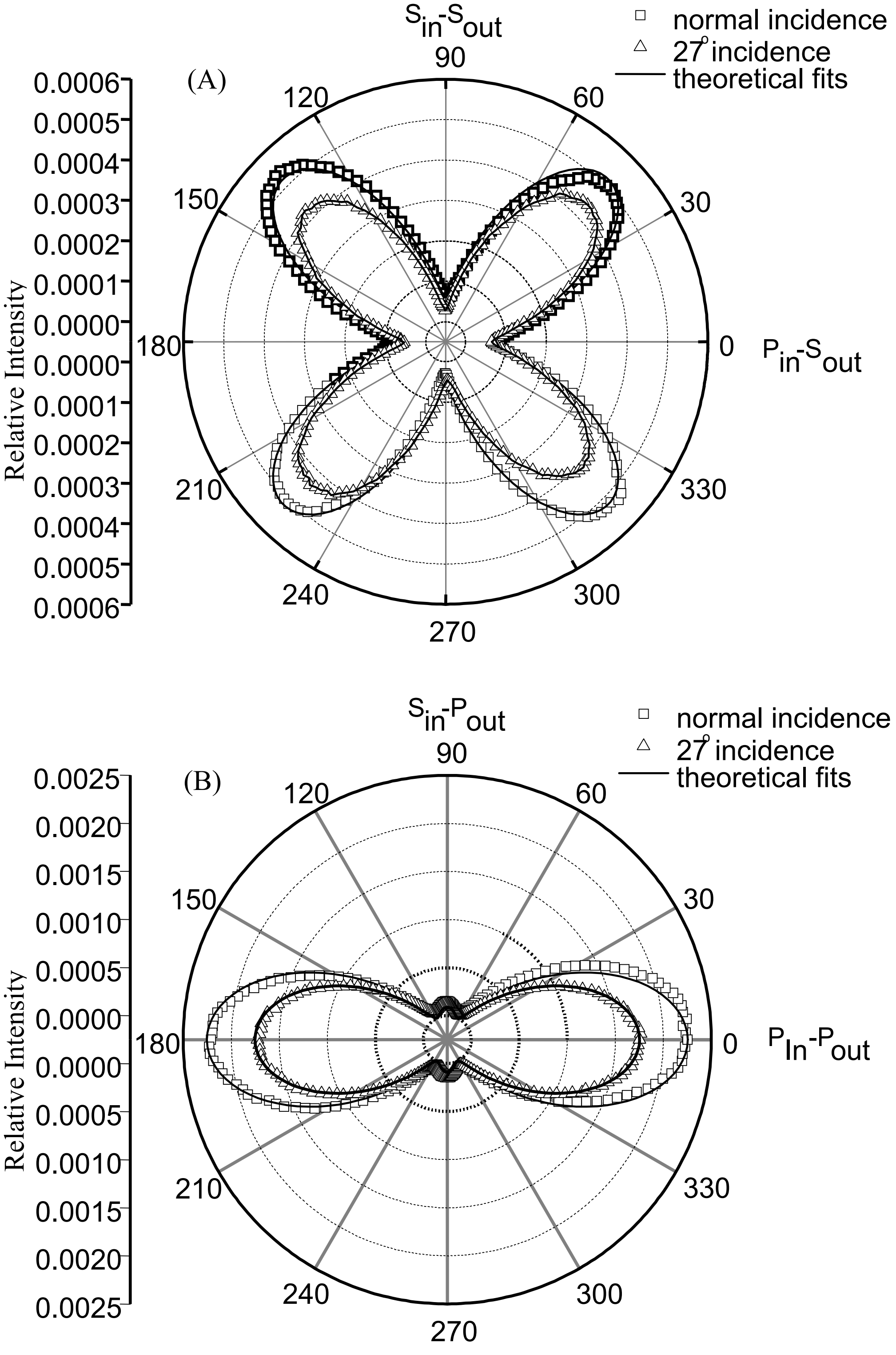

Figure 3: Polarization diagrams for a sample ZnO rod from Geren et al.[21]

The values for the fitting parameters a_p and b_p used in the theoretical fit in Figure 3(B) were inserted into Equation 15 for both normal incidence and an incidence of 27º. From these equations, the tensor component ratios were found to be d_{33}/d_{31}= -5.4 and d_{15}/d_{31}=1.53. The ratios showed that not only was d_{33} the dominant component of the tensor as indicated by the greater amplitude, but also that it was opposite in sign to the other components. The magnitude found for d_{33}/d_{31} was similar to the magnitude of 4.2 reported for similar ZnO structures using the NSOM method, while the negative sign was consistent with the ratios found for bulk ZnO crystals.[17,25] The sign of the ratio was not accounted for in the NSOM method. The value found for d_{15}/d_{31} indicates that Kleinman's symmetry, which has been assumed in most previous methods of measurement, is not followed at this wavelength. This is most likely caused by absorption of the second harmonic radiation as the second harmonic radiation has an energy only slightly lower than that of the bandgap of ZnO. This has previously been observed in ZnO thin films.[18] Neither Equation (14a) nor Figure 3(A) were used to find these ratios, but the good correspondence between the two indicates that the theory is valid. The refractive indices of the rod and substrate used to calculate these ratios were N_2=1.470, n_2=1.453, N_3=2.1708, and n_3=1.9407 for the substrate and rod respectively.

In order to find magnitudes for the elements d_{33}, d_{31}, and d_{15}, the second harmonic intensity for a reference material with known susceptibility components was measured. For the purpose of this measurement, the ZnO rod sample was replaced in the experimental setup with a Z-cut quartz plate oriented $\left[1 \quad 0 \quad \bar{1} \quad 0\right]$ along the $\hat{k}$ direction. The p-polarized second harmonic intensity from the quartz plate, I^{q}_{p-p}, was compared to the p-polarized second harmonic intensity from the ZnO rod , I^{NR}_{p-p}. Both of these intensities were measured under the condition of a p-polarized fundamental beam with normal incidence. The ratio of the intensities of the second harmonic from the ZnO rod and quartz plate were estimated as follows: an objective and camera were placed behind the polarizer in the experimental setup and the ratio $I_{p-p}^{NR} / I_{p-p}^{q}$ was determined by measuring the brightness at the center of each image. Using this ratio, the magnitude of d_{33} was determined using the following equation:

(Equation 16)

$$d_{33} = d_{11}^{q} \left| \frac{t_{\omega}^{v \to q}}{t_{\omega}^{p}} \right|^{2} \left| \frac{2N_3 (N_3 - n_3)}{(N_q - n_q)(1 + N_q) T_{34,2\omega}^{p}} \right| \times \left| \frac{1}{1 - \exp[-i2\omega / cD(N_3 - n_3)]} \right| \times \left(\frac{I_{p-p}^{NR}}{I_{p-p}^{q}} \right)^{1/2},$$

using the values N_q=1.55713, n_q=1.53822, and $d_{11}^{q} = 0.3$ pm/V.[26]

From the above equation, d_{33} was found to be 3 pm/V. This value is of the same order of magnitude as the value d_{33}= 5.5 pm/V found previously for ZnO wires using the NSOM method.[17] Using the ratios d_{33}/d_{31}=-5.4 and d_{15}/d_{31}=1.53, the values d_{31}=0.56 pm/V and d_{15}=0.86 pm/V were calculated. The similarity of these values to the previous results seen for ZnO nanowires indicates the validity of this method. The values found for the nonlinear coefficients in this work are not meant to be accurate as their purpose was to prove the method, though the polarization data the values were derived from had a precision within the markers of Figure 3 for the specific setup used.

Chapter 3: Imaging Second Harmonic Radiation in ZnO Rods

As mentioned previously, Liu et al.[20] introduced a model for ZnO rods that represents the rods as dipoles. Each rod is modeled as an infinitely thin dipole wire of the same length as the ZnO rod. The intensity pattern of the far field second harmonic scatter is compared to the time averaged Poynting vector of the dipoles calculated from the following equation: [20]

(Equation 17)

$$S_z^{2\omega}(x,y,d_{eff}) = -\frac{1}{2\mu_0}\mathrm{Re}\left[\int_{-L/2}^{L/2} E_z^{2\omega}(x,y,d_{eff},y')^* \, dy' \times \int_{-L/2}^{L/2} B_y^{2\omega}(x,y,d_{eff},y')dy'\right].$$

In this equation, the E and B fields are described by

$$E_z^{2\omega} = \pm\left[\sin^2\theta + (3\cos^2\theta - 1)(1/r^2 - 2i\,\omega/c/r)/(2\omega/c)^2\right]e^{\,i2\omega//cr}/r \quad ,$$ (Equation 18)

$$B_y^{2\omega} = \pm\sin\theta\cos\phi\left[c/(2i\omega r) - 1\right]e^{\,i2\omega/cr}/r\,,$$ (Equation 19)

with the variables defined as follows,

$$r = \left[x^2 + (y-y')^2 + d_{eff}\right]^{1/2},$$ (Equation 20a)

$$\sin^2\theta = \left(x^2 + d_{eff}^2\right)/\left[x^2 + (y-y')^2 + d_{eff}^2\right],$$ (Equation 20b)

$$\cos^2\phi = d_{eff}^2/\left(x^2 + d_{eff}^2\right).$$ (Equation 20c)

L is the length of the rod and d_{eff} is a fitting parameter relating to the optical path length. The ± sign at the beginning of the field equations is used to indicate the direction of the dipole. In the case of the twinned dipoles, the sign is reversed at the center of the dipole. The coordinate system for this work's simulations was set up as seen in Figure 4.

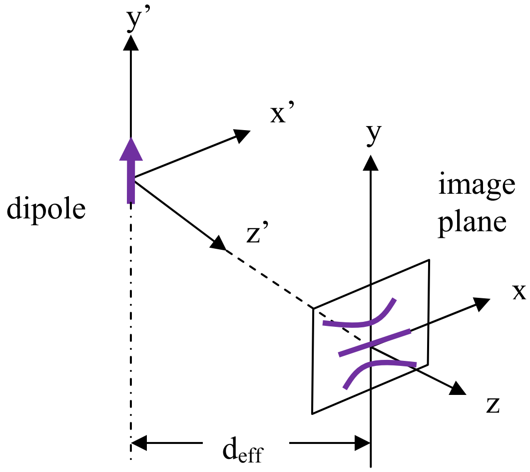

Figure 4: Coordinate system of the dipole simulations.

The experimental images of the second harmonic intensity scatter patterns from the ZnO rods were obtained using a 1 watt mode locked Ti:Sapphire laser with a wavelength of 810 nm for an excitation source. The laser beam was passed through a lens (L; Φ=1in, f=20cm) to focus the beam onto the rod sample (S) and then a long pass filter (LF; 650-2200 nm) to remove any incident second harmonic from the beam. After the sample, a band-pass filter (BF; 350-650 nm) was used to select for only the second harmonic radiation. This radiation was then focused as a planar image on a digital camera using an objective (OB; 50x magnification f=200) and a flat mirror (M) as can be seen in Figure 5.

The results from Liu et al.’s simulations and experimental images show that the images of the magnitude of the time averaged Poynting vector of the dipole are consistent with the intensity patterns of the far field second harmonic scatter from the rods. They both show strong fringing from interference along the length of the rod with the number of fringes increasing with the length of the rod.

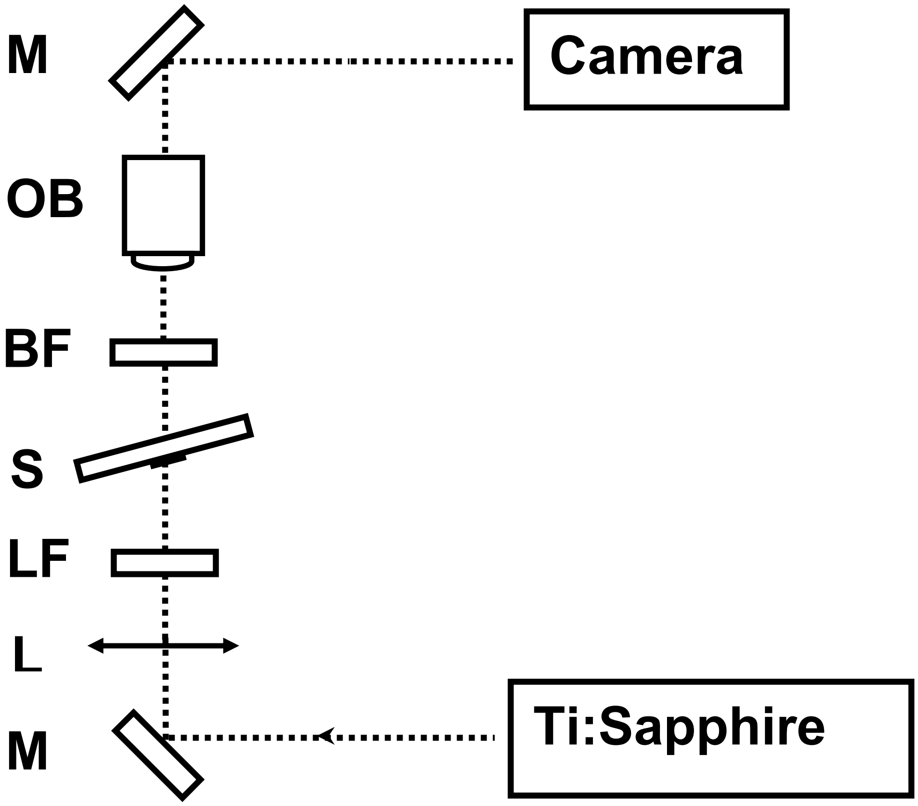

Figure 5: Top view of the experimental layout on an optical table for acquiring second harmonic scattering images.

The number of fringes for a particular length rod is the same as that for a dipole of that length. A bright or dark fringe along the central orthogonal axis of the rod indicates either an untwinned rod or a twinned rod respectively. Twinning refers to a crystal defect in which the polarity of the crystal is 180 degrees out of phase for the two halves of the crystal.

In order to repeat these simulations, a Matlab program was created to calculate the time averaged Poynting vector for the finite dipoles and plot the magnitude of this vector in the viewing plane. A flow chart of this program can be seen in Figure 6.

When the results from this program, Figure 7(A) were compared against the experimental results and simulations from the source, it was seen that the shape and number of fringes were consistent for a given dipole/rod length and that twinning was accurately predicted as a dark central fringe in the dipole model. While the second, dimmer fringe was not seen in the figure, it did appear numerically in the results but the resolution of the rendering program was not high enough to show it here. Figure 7 shows the experimental and simulated patterns found by Liu et al. for a 1.5 μm rod.[20]

In order to more easily simulate more complicated structures, the model had to be converted to vector format. This was accomplished by simply replacing the scalar equations with the customary vector dipole equations for the electric and magnetic fields and integrating these over a finite length. The Matlab program for this can be seen in Appendix A. The equations used were,[27]

$$H = \frac{ck_2^{\,2}}{4\pi}(n\times p)\frac{e^{ik_2 r}}{r}\left(1-\frac{1}{ik_2 r}\right), \qquad \text{(Equation 21)}$$

$$E = \frac{1}{4\pi\varepsilon_0}\left\{k^2(n\times p)\times n\frac{e^{ik_2 r}}{r} + \left[3n(n\cdot p)-p\right]\left(\frac{1}{r^3}-\frac{ik}{r^2}\right)e^{ik_2 r}\right\}. \qquad \text{(Equation 22)}$$

It can be seen from

Figure 8 that the results of these simulations were again consistent with the earlier images in Figure 7 in shape and number of fringes.

This model can therefore be used for more complex structures with some confidence. Figure 8(B) had the resolution of its color map altered to show the second dimmer fringe of the structure. The parameters for the simulation depicted in Figure 8 were a length of 1.5 μm and an effective distance d_{eff} of 18 μm.

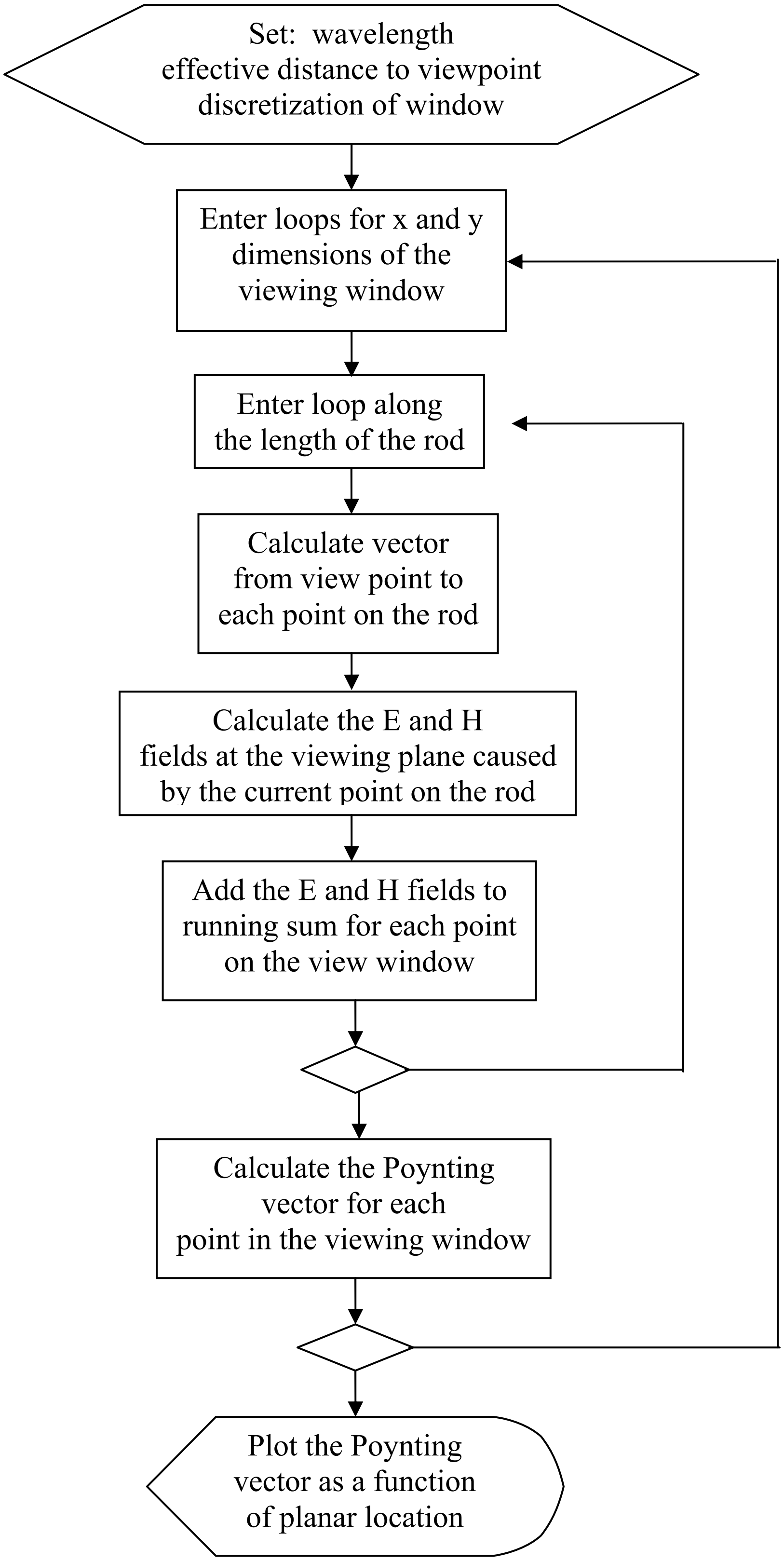

Figure 6: Flow chart of dipole simulation program.

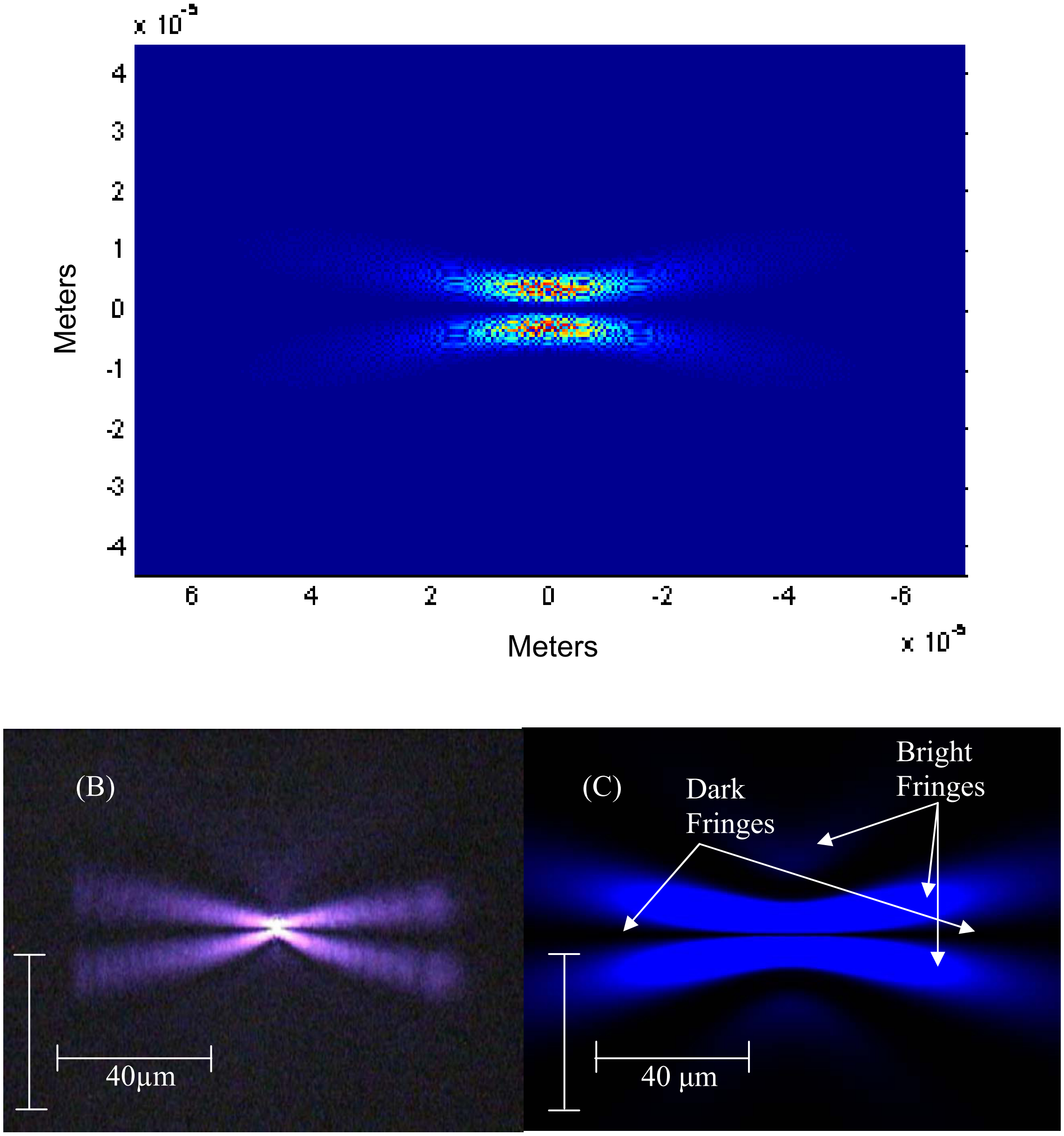

Figure 7: Simulated image of the dipole Poynting vector (A), experimental image of second harmonic scatter from Liu et al (B), and simulated image of the dipole Poynting vector from Liu et al (C).[20]

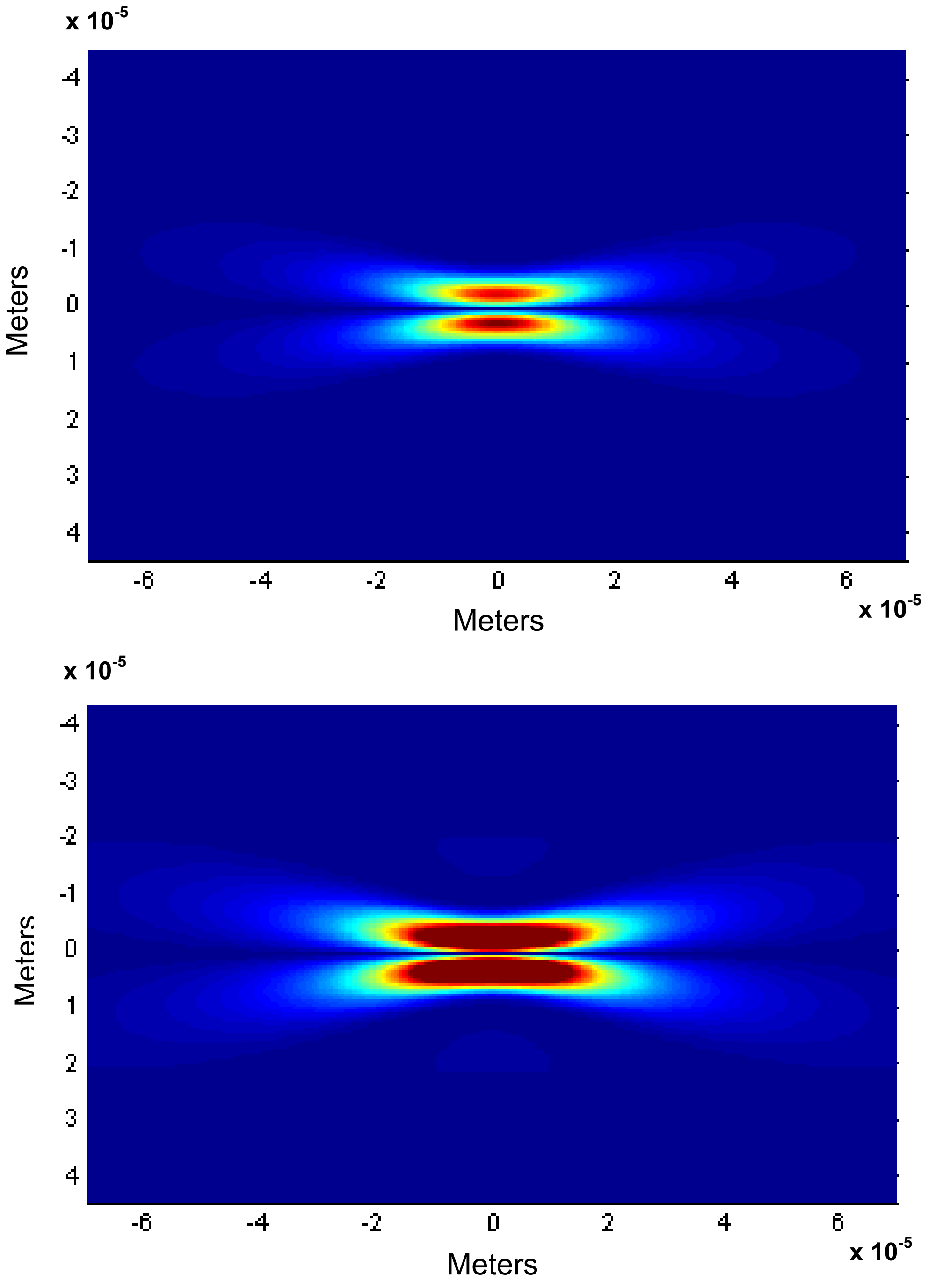

Figure 8: Vector simulation of a dipole rod in: original resolution (A) and adjusted resolution (B).

Chapter 4: Radiation Patterns of More Complex Structures

4.1 Two Joined Rods

The first more complex structure investigated was that of two rods joined at an angle of 120°. This sample was created with a batch of tetrapods and is most likely either part of a tetrapod that did not completely form, or part of a tetrapod that was damaged before it was viewed. An image of a typical tetrapod sample can be seen in Figure 9.

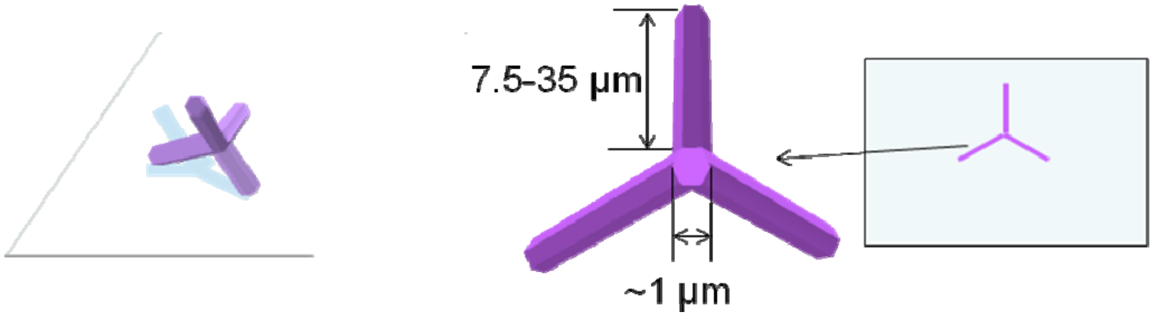

Figure 9: Typical Example of tetrapod samples.

The tetrapod samples were created using a direct thermal evaporation and condensation process and dispersed into water to get the desired low sample density. The water suspension was applied to a fused quartz plate for viewing. The samples were once again prepared by Dr. Huajun Zhou.

Experimental images of the second harmonic scatter for the joined rod structure were obtained using the same experimental setup detailed in Figure 5 for the nanorods. A number of different models were used to simulate this structure before one produced a reasonable replica of the experimental radiation pattern.

The first model used was two untwinned dipoles joined at an angle of 120° (as seen in Figure 10) set in a plane parallel to the viewing plane.

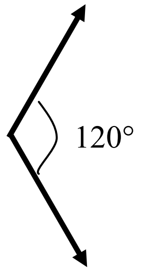

Figure 10: Planar model of two joined rods.

This was created by integrating the dipole field equations along two vectors separated by 120° simultaneously and then looking at the effect of both dipoles on each point of the viewing plane. This model resulted in a fairly predictable composite of two standard dipole patterns overlapping each other. As shown in Figure 11, the primary features of the results of this model were two bright fringes corresponding to the centers of each individual rod respectively, set apart by an angle of 120° with the darker fringes forming a grid pattern between the two primary fringes. This pattern bore almost no resemblance to the experimental image of this structure as shown in Figure 12.

Strangely, a model created by mistake in which the dipole moment did not follow the vector of the axis of the ZnO rods, but was perpendicular to the axis, actually did bear resemblance to the experimental image. As seen in Figure 13, the details did not match but the basic shapes of the patterns were remarkably similar. The patterns show the same channel-like structure surrounding a central arrow shaped spot. The difference between the experimental and simulated images lay primarily in the weighting of the individual elements of the patterns. The simulated image showed the edges as brighter, while the experimental image showed the center as brighter.

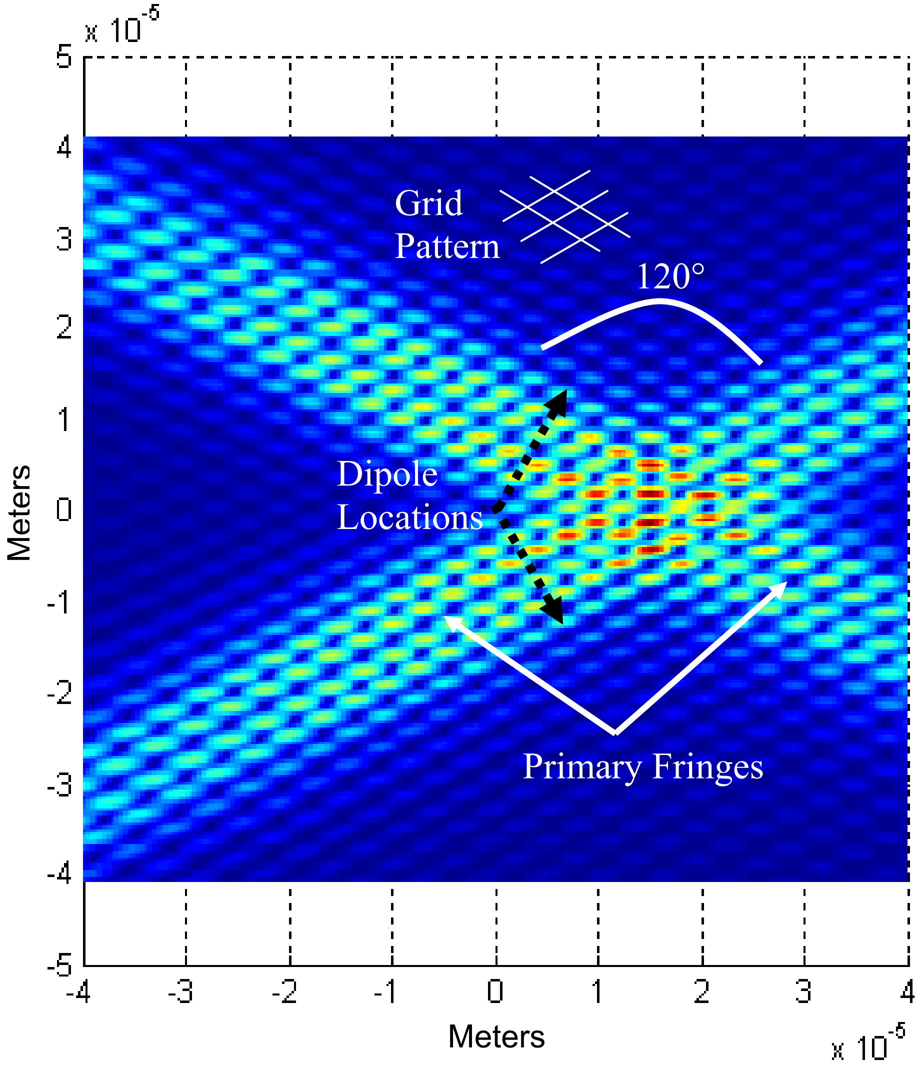

Figure 11: Simulation of two joined dipoles.

While this model ded show so much similarity to the experimental image, it was not valid as it did not reflect the physical structure of the ZnO rods. ZnO has a hexagonal crystal structure which causes its polarity to be directed along the z-axis of the crystal which lies along the length of the rod.

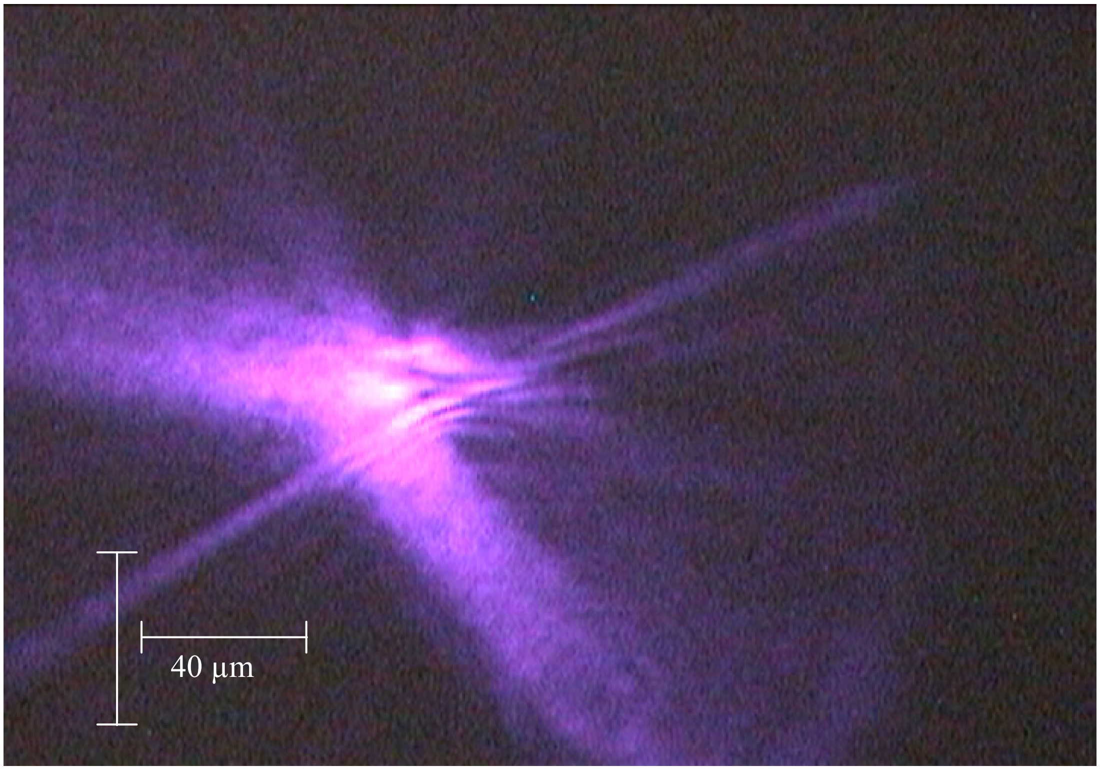

Figure 12: Experimental second harmonic scattering pattern for two joined rods.

The fact that these patterns were so similar indicated that something was not being taken into account correctly in the model. The similarity could be caused by the change in the direction of the polarization with location, which could indicate the need for the addition of the third dimension to create a similar effect. A less likely, but more easily verified, reason for the lack of similarity between the more physically accurate simulation and the experimental images might be that the affect of the susceptibility vector was not accounted for in this simulation.

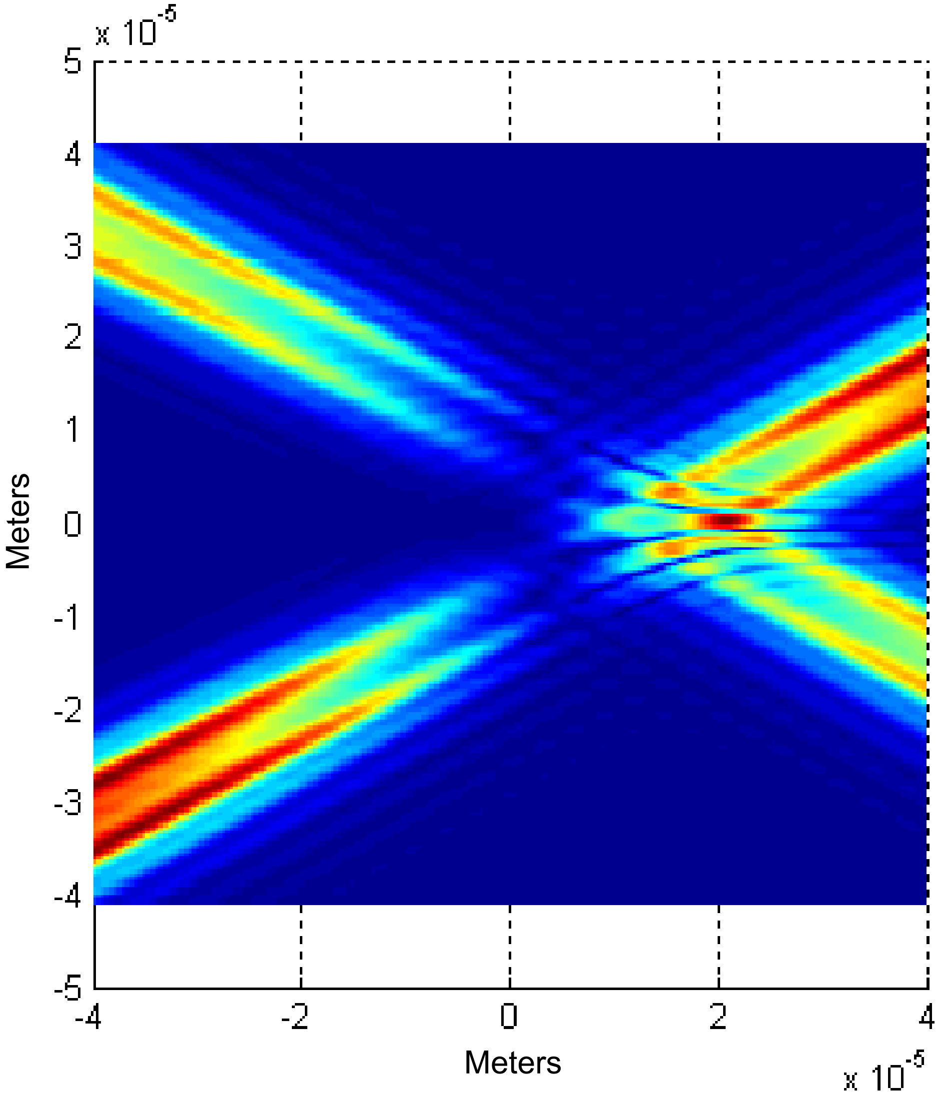

Figure 13: Simulation results for two joined rods with the dipole moment directed perpendicular to the length of the rod.

The effect of the susceptibility vector was easily estimated by simply multiplying the electric field for each leg of the structure by the square of an effective susceptibility constant, χ_{eff}. The effective susceptibility for each leg of the structure was individually estimated using the following equation:

$$\chi_{eff} = 2d_{15}\cos\theta\sin\theta + d_{31}\sin^2\theta + d_{33}\cos^2\theta . \qquad \text{(Equation 23)}$$

The variable θ is defined as the angle between the rod axis and the vertical polarization of the incident laser beam. The values for the nonlinear coefficients in this equation were taken to be the values presented in Chapter 2 of this thesis. Equation 23 was derived by applying the assumed geometric orientation of the rod as represented in Figure 14 to the polarization tensor.

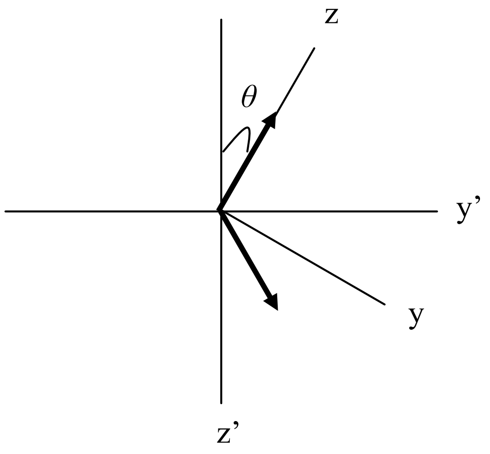

Figure 14: Assumed geometric orientation of the joined rod model.

There was no real justification for the orientation of the y direction as in the plane of the structure and the x direction as perpendicular other than it was a convenient orientation for calculating the estimate. The crystalline z direction was known to be along the axis of the rod as shown. Because the polarization of the fundamental beam was along the z' axis and the z component of the susceptibility tensor, d_{33}, was the dominant component, the angle between these two directions (θ) should be the most influential in the weighting of the radiation of each rod due to the susceptibility of the crystal, making Equation 6 a reasonable estimate.

The inclusion of this susceptibility weighting in the model did not seem to have much effect on the simulation. This image was not included in this document because it was quite similar to Figure 11 in all but a slight difference in the intensity of certain parts of the pattern. The simulated and experimental radiation patterns for the two joined rods still do not show similar primary characteristics. The simulated pattern primarily consisted of a grid-structure while the experimental pattern showed an arrow-like structure.

There were several possible reasons for the continuing lack of similarity between the simulation results and the experimental images. The most obvious was that the exact orientation of the experimental structure was not known. This problem was not easily fixed and thus was ignored. Another reason was the possibility that the rods were acting as waveguides and distorting the image. This theory was not able to be easily tested. The difference could also be caused by defects in the experimental sample. This probably did cause some aberrations in the experimental scatter patterns, but the global nature of the differences indicated that this was not the primary reason. The most likely reason for the differences in the patterns was that the current model assumed that the structure was planar and lay in a plane parallel to the viewing plane. This was not truly the case for the experimental structure. Given the earlier findings with the non-parallel model this seemed a likely avenue to pursue. This was fairly easily accomplished given the vector nature of the model.

Basically the third dimension was added into the unit vectors in the model. This version of the model was much more closely related to the experimental data. The simulated scatter pattern from this modeled shared the arrow-like structure of the experimental structure. When the susceptibility estimates derived for the planar model were added into the current model the images became even more similar as seen in Figure 15 with the lower leg showing brighter second harmonic fringing. The susceptibility estimates were still fairly valid estimates as the differences in the models occured in the x and y directions which were assumed in the original equation anyway. Therefore this estimate was as valid as the last. The image in Figure 15(B) represents a model assuming an angle of 120° between the legs in the y'-z' plane and each leg slanted back at an angle of -30° back from that plane. The legs were placed in the 1st and 4th quadrants each with a length of 12 μm. The susceptibility weightings were 2.4 and 2.8 respectively.

As can be seen in Figure 15, the shapes of the patterns match quite well. Even the weighting of the components of the patterns were similar. The number of bright fringes matched on the bottom half of the patterns though not on the top. The length of the legs was actually estimated to within 10% of the actual value using this model prior to the measurement of their length. The offset of the pattern from the location of the structure did not seem to quite match as the simulated pattern occurred almost twice as far to the right of the structure as in the experimental pattern, but this offset was highly dependent on the angles the legs made with the various coordinate axes.

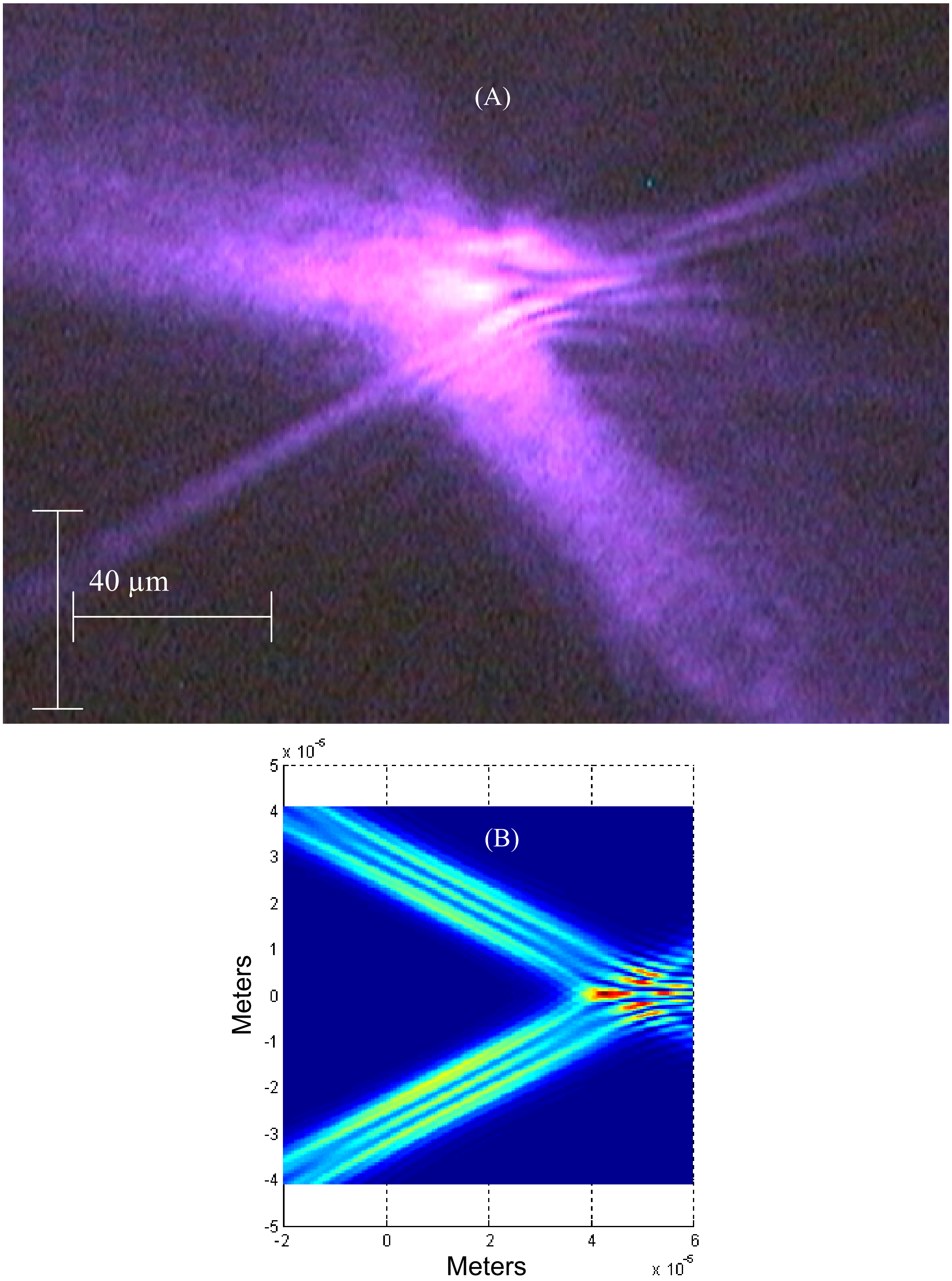

Figure 15: Comparison between the experimental image (A) and the 3D simulation results (B) for two joined rods.

The angles used in the model were unfortunately not very accurate, which would explain the difference in the offset. The angles used were the midpoint of the most likely location as suggested by the geometry of a typical tetrapod. The angle between the legs of 120 degrees was chosen because of the assumption that the structure would follow the shape of the tetrapods. This is likely, but not certain. Also, the effective distance used in the model is not necessarily correct as it is used as a fitting parameter. Though the patterns are similar, details did not exactly match as detailed above. This was most likely caused by the inexact angles and possibly defects in the crystal structure of the sample.

If crystal defects were to blame for the differences in the patterns, it was possible that the rods making up the structure are twinned. This possibility was investigated using the three dimensional model. The model was altered so that the polarity of the dipoles making up the legs reversed at the center of the rod as seen in Figure 16. The same susceptibility weighting and leg length as used in the last simulation were used.

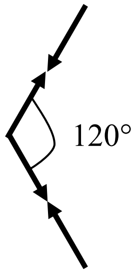

Figure 16: Setup of twinned model of two joined rods.

When the results of this simulation were compared with the experimental image of the two joined rods in Figure 17, it was seen that there was once again very little resemblance.

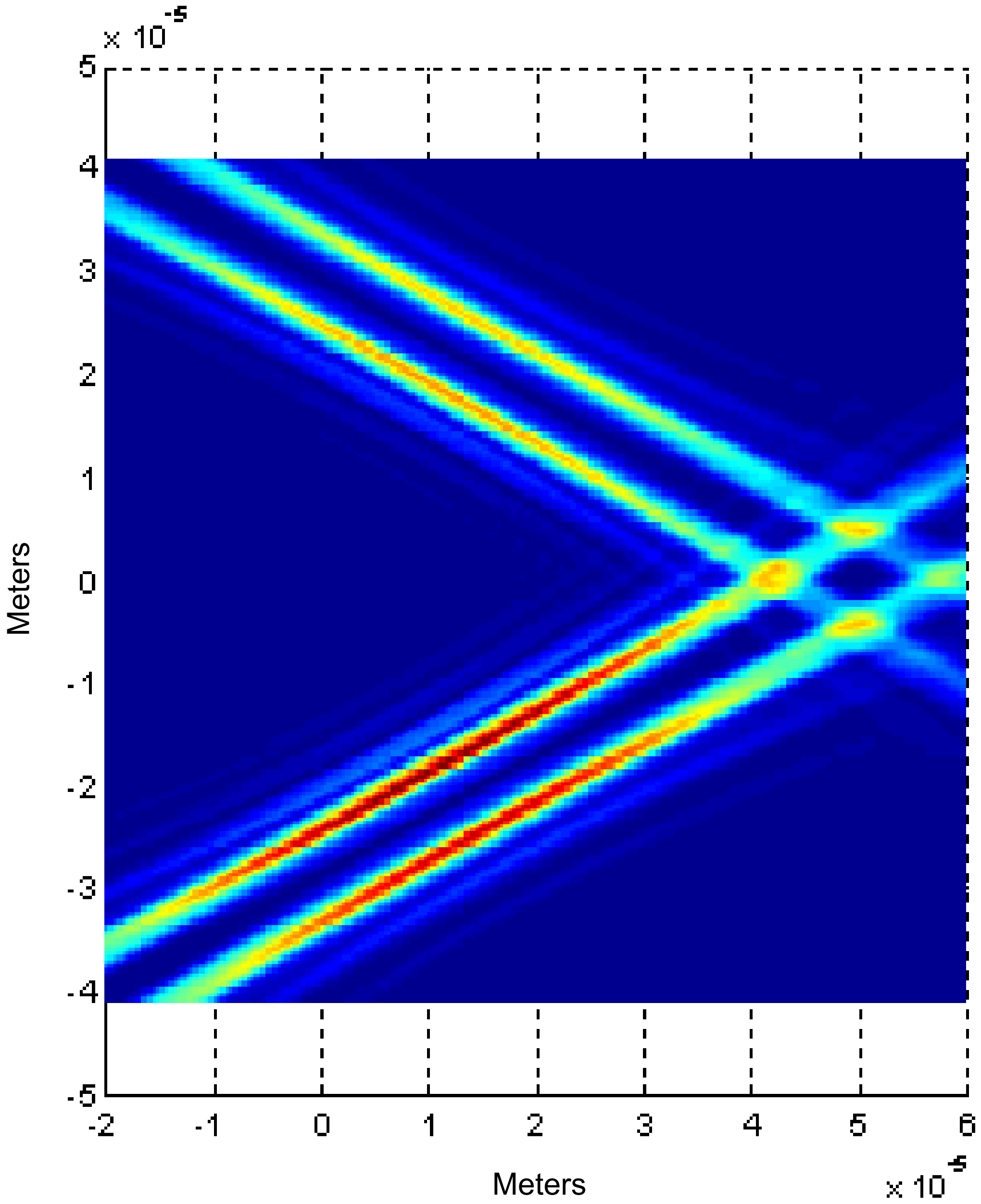

Figure 17: Results from three dimensional simulation of two twinned joined dipoles.

The simulation showed intersecting dipole patterns forming a somewhat diamond shape in between the rods, where as the actual experimental image showed more of an open triangle shape. Addition of the susceptibility weighting did not improve the similarity.

The experimental data most closely matched the untwinned three dimensional model of two joined dipoles as seen in Figure 15. The addition of twinning to the model in Figure 16 seemed to move the images much further apart, indicating that the experimental structure probably did not contain a twinning plane. Given the favorable results seen for this structure, comparisons with more complicated structures seemed feasible, though with the larger number of variables the accuracy of the model was expected to decrease.

4.2 Tetrapod

The next structure modeled was a tetrapod with one leg pointed perpendicular to the viewing plane and the polarization of the incident laser beam. The perpendicular leg was expected to have negligible affect on the model as it should not be excited by the incident beam due to its crystal polarization being perpendicular to the polarization of the incident laser beam. A description of the sample preparation can be seen in Section 4.1.

The first model used to describe the tetrapod was a planar Y-formation of three dipoles. The model consisted of three outward pointed dipoles joined at their bases as seen in Figure 18.

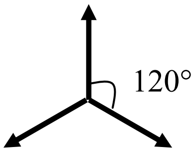

Figure 18: Planar Y-formation model.

The results of this model once again formed a grid pattern centered around the three central fringes of the dipoles. As can be seen from Figure 19, there is very little resemblance between the experimental scattering images and the simulation results. This was expected after the earlier lack of success with the planar model. The addition of twinning to the model, similar to what was done in Figure 16, also did not increase the match between the experimental and simulated images.

After the expected failure of the planar model, the third dimension was added to account for the slant of the legs, though the fourth leg was still ignored as seen in Figure 20.

The same equation was used to estimate the effect of the susceptibility as described in Section 4.1. The Matlab program for this model can be seen in Appendix B. The results of this model placed a great deal of emphasis on the scatter from the vertically aligned dipole. This was because the vertically polarized fundamental beam coupled most strongly into this leg. The most noticeable feature of the simulation results as seen in Figure 22 was the overall triangular shape of the pattern. Neither of the experimental images showed the dark triangle at the center of the pattern that was prominent in the simulation. This was partially explained by the fact that the simulation did not show the structure itself, which was directly in the middle of that dark area. The difference in the two experimental images was due to the difference in focus between the two pictures. Taking the actual structure out of the focus of the image often makes the pattern clearer. The image in Figure 21(A) was focused in front of the tetrapod with a length of 7.9 μm, while the image in Figure 21(B) was focused on the tetrapod with a length of 13.8 μm. The simulation in Figure 22 assumed a dipole length of 13.8 μm. In this case, there was more similarity seen with the focused image. This was probably because the structure more closely resembled the model geometry. The intersection of the dipole patterns were faintly seen at the corners of the experimental image.

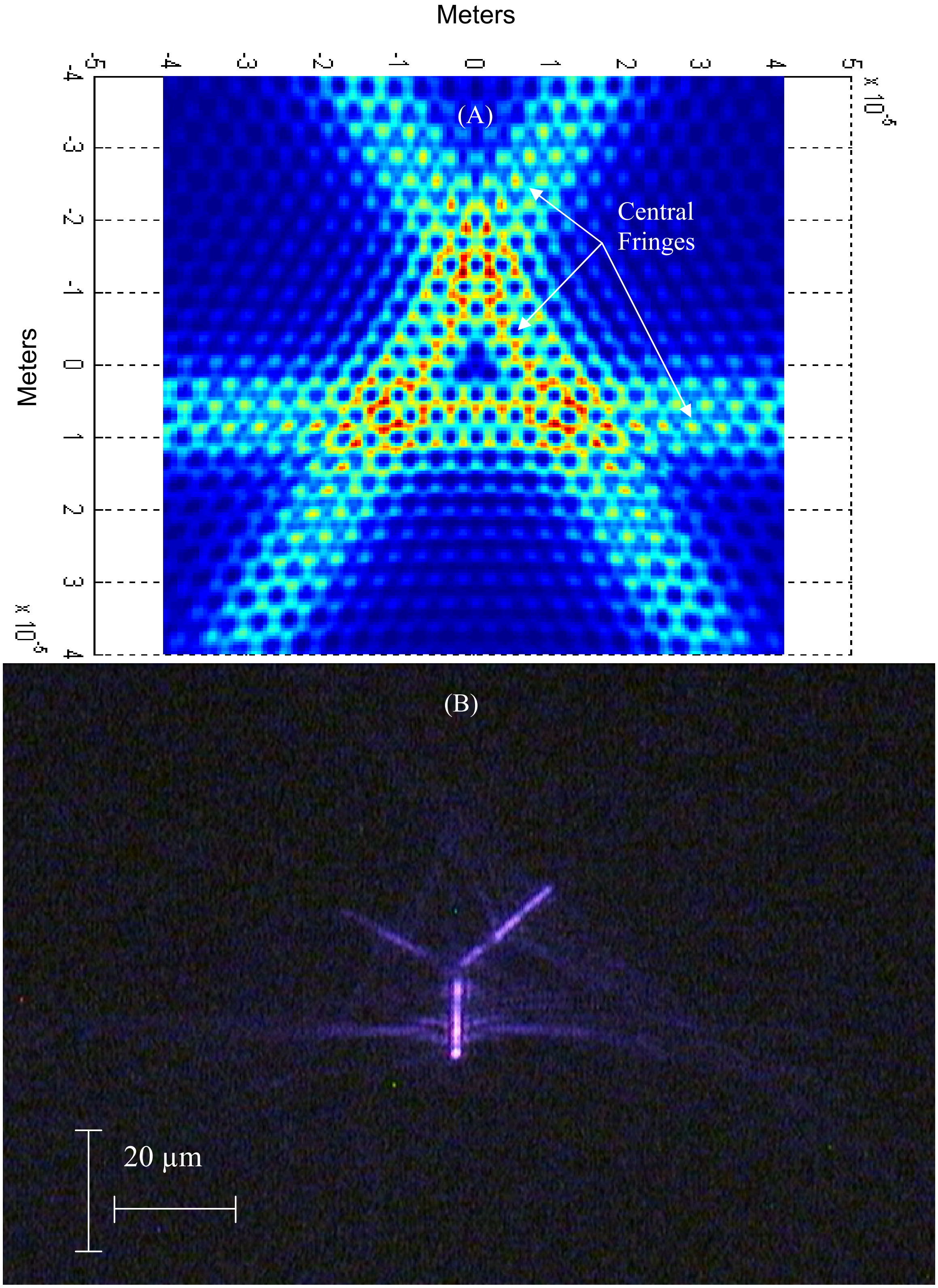

Figure 19: Two dimensional tetrapod simulation (A) compared with experimental tetrapod second harmonic pattern (B).

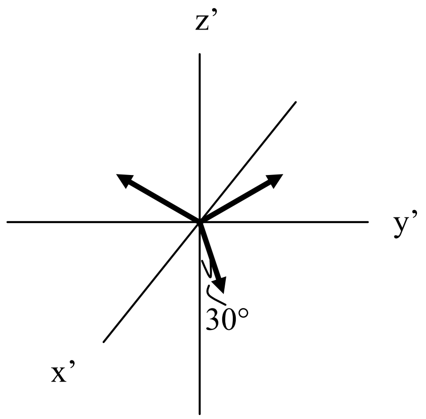

Figure 20: Tetrapod model.

The experimental image also appeared to have a faint overall vaguely triangular shape as seen in the simulation. Even so, the experimental images were not a good match to the simulation. This could have been caused by several factors. First, the alignment of the tetrapod was not exact. The fourth leg was probably not exactly perpendicular to the fundamental polarization, which would skew the results. Also, if one leg was more parallel to the viewing plane than the others, this would add additional weight to that scatter. Also, the tetrapod did have some defects which would also skew the image.

In an attempt to be thorough, a last simulation was performed with twinned dipoles. This produced the pattern seen in Figure 23 with more defined striations and a grid pattern between the primary fringes. This bore little resemblance to the experimental images seen in Figure 21(A) and Figure 21(B). The grid-like pattern resembled the first experimental image in Figure 22, but the distinctive double fringes were absent from the experimental images. This indicated that not every leg of the tetrapod was twinned or that there were no twinning planes, but that other defects were present.

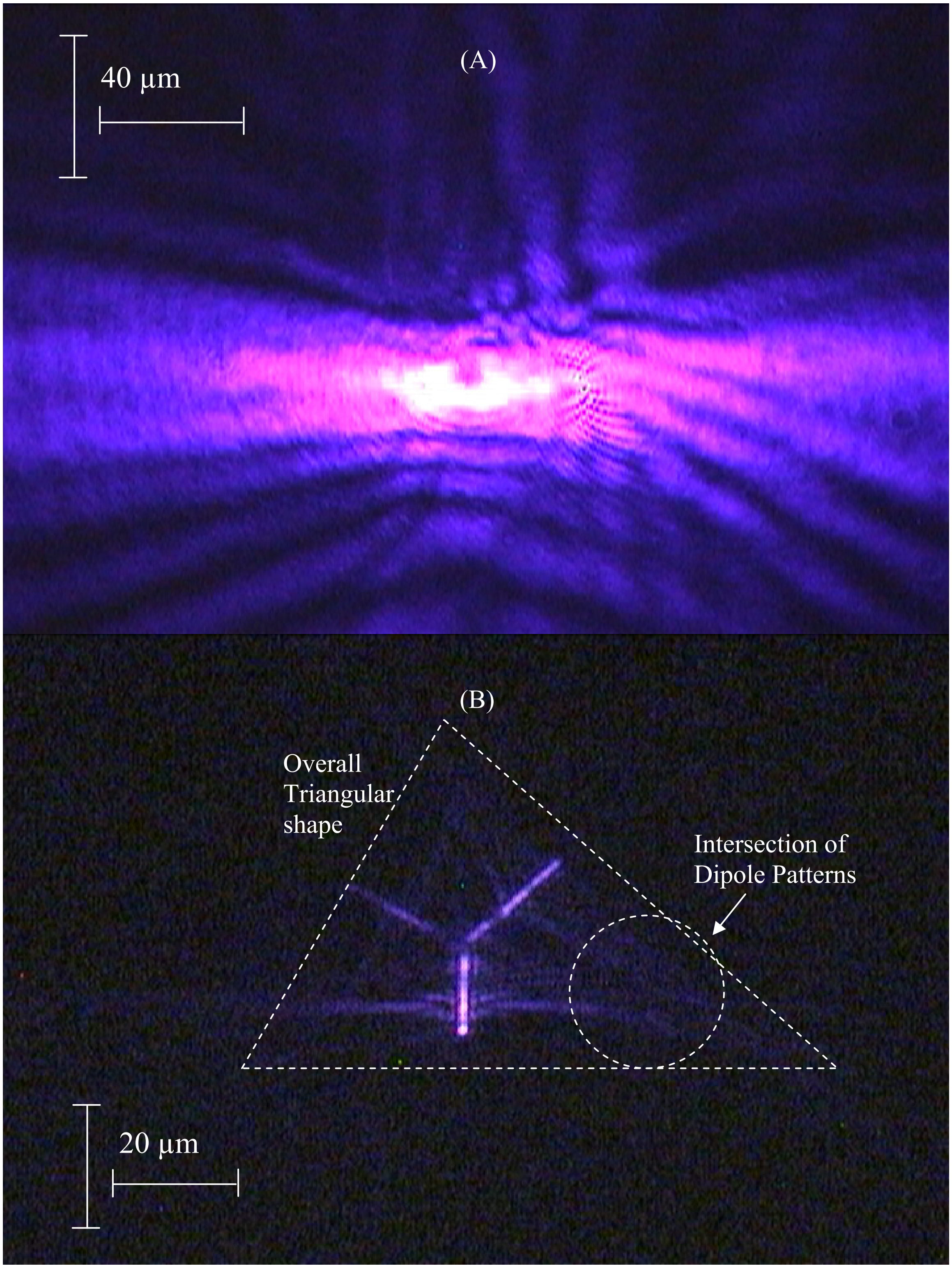

Figure 21: Experimental second order scatter patterns from a 7.9 µm tetrapod (A) and a 13.8 µm tetrapod (B).

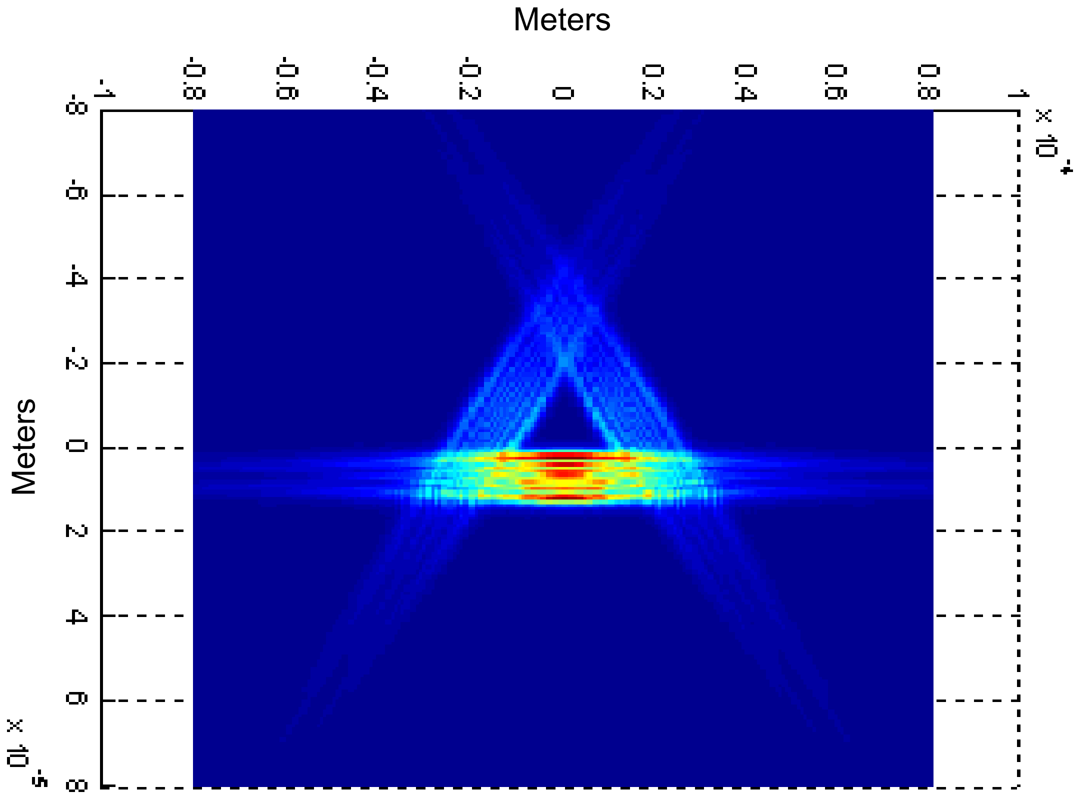

Figure 22: Three dimensional simulation of 13.8 µm tetrapod.

Despite the similarities seen, this model still did not give an accurate picture of the scattering patterns of tetrapods, though it was possible that the experimental setup was not exact enough to define the geometric orientation well enough for an accurate model.

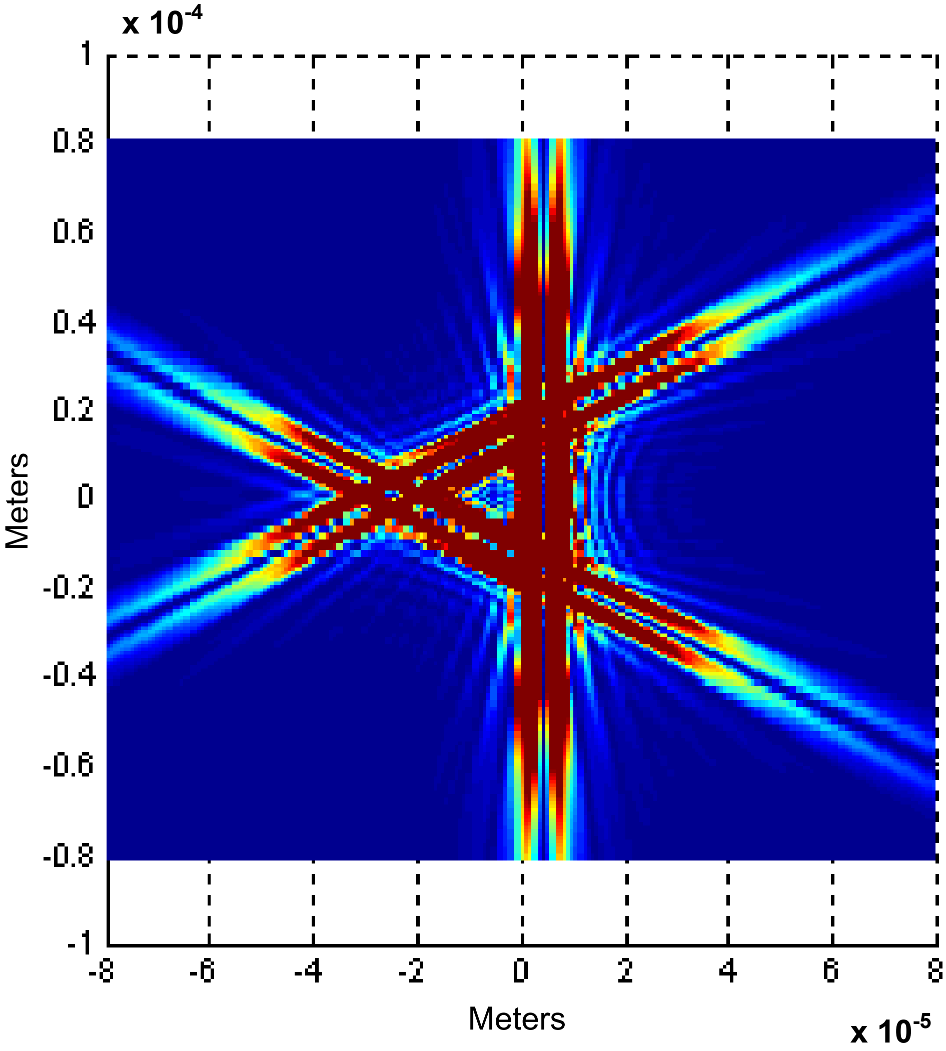

Figure 23: Three dimensional simulation of twinned dipoles with a length of 8 µm.

Chapter 5: Other Experimental Results

5.1 Propagation of Light Through Structures

Another experiment was performed in an attempt to investigate the propagation of the second harmonic through the structure. Some parts of the second harmonic scattering pattern were not well explained by the model presented in the previous section. For example, many of the structures showed a periodic series of bright spots in the scatter along the length of the rod. It was suggested that these spots might have something to do with either the propagation of the light through the structure or some sort of resonant activity. Perhaps this could be seen more clearly if the excitation beam did not overlap the phenomenon.

Previously propagation of photoluminescence through tetrapods has been reported by Zhang et al.[11] This source did not report any propagation of the excitation beam through the structure. They showed a faint luminescence throughout the structure due to leakage, but did not report any of the periodic structure seen in many of this work's images. Evidence of waveguide activity has also been reported from lasing characteristics of tetrapods.[12]

For this investigation, the earlier experimental setup was slightly modified by replacing the focusing lens with a focusing objective (OB; 50x magnification, f=200) in order to reduce the spot size below the size of the structures. The spot size on the sample was approximately 5 μm. An attenuator (AT) was also added between the laser and the sample at times so as not to destroy the sample. It was set just high enough to achieve this purpose (this was indicated by the glare from the screen not bleaching the colors of the pattern). A polarizer (P) was added in front of the camera for some parts of the investigation as seen in Figure 24.

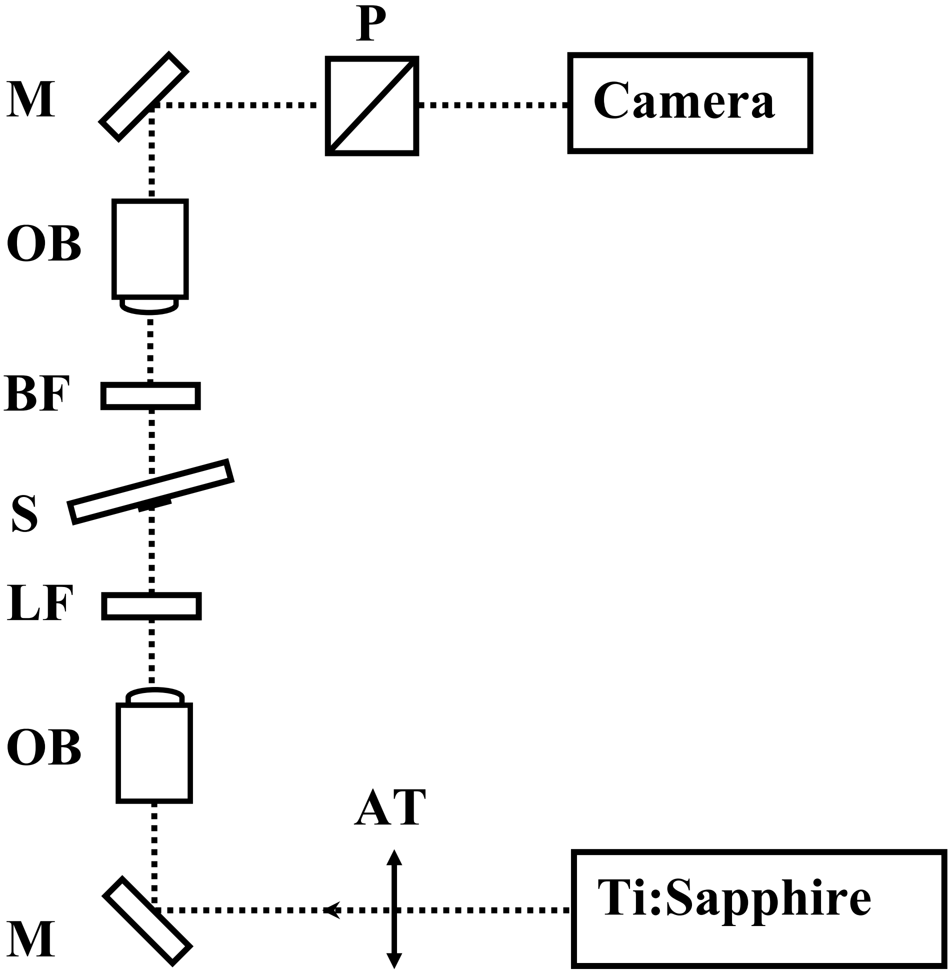

Figure 24: Experimental setup for investigating propagation

This setup was used to excite just one section of the sample structure with the laser. The entire structure was then imaged, paying particular interest to the sections of the structure that were not directly excited.

The most interesting result was acquired from another partial tetrapod. Only one leg of the tetrapod was illuminated with the fundamental beam, but scatter was observed from the end of the other leg as seen in Figure 25. The scatter from the two legs was out of phase by 110º ±10°. This seemed to correspond with the angular separation of the legs. It was not determined whether it was the fundamental or second harmonic light which propagated through the structure.

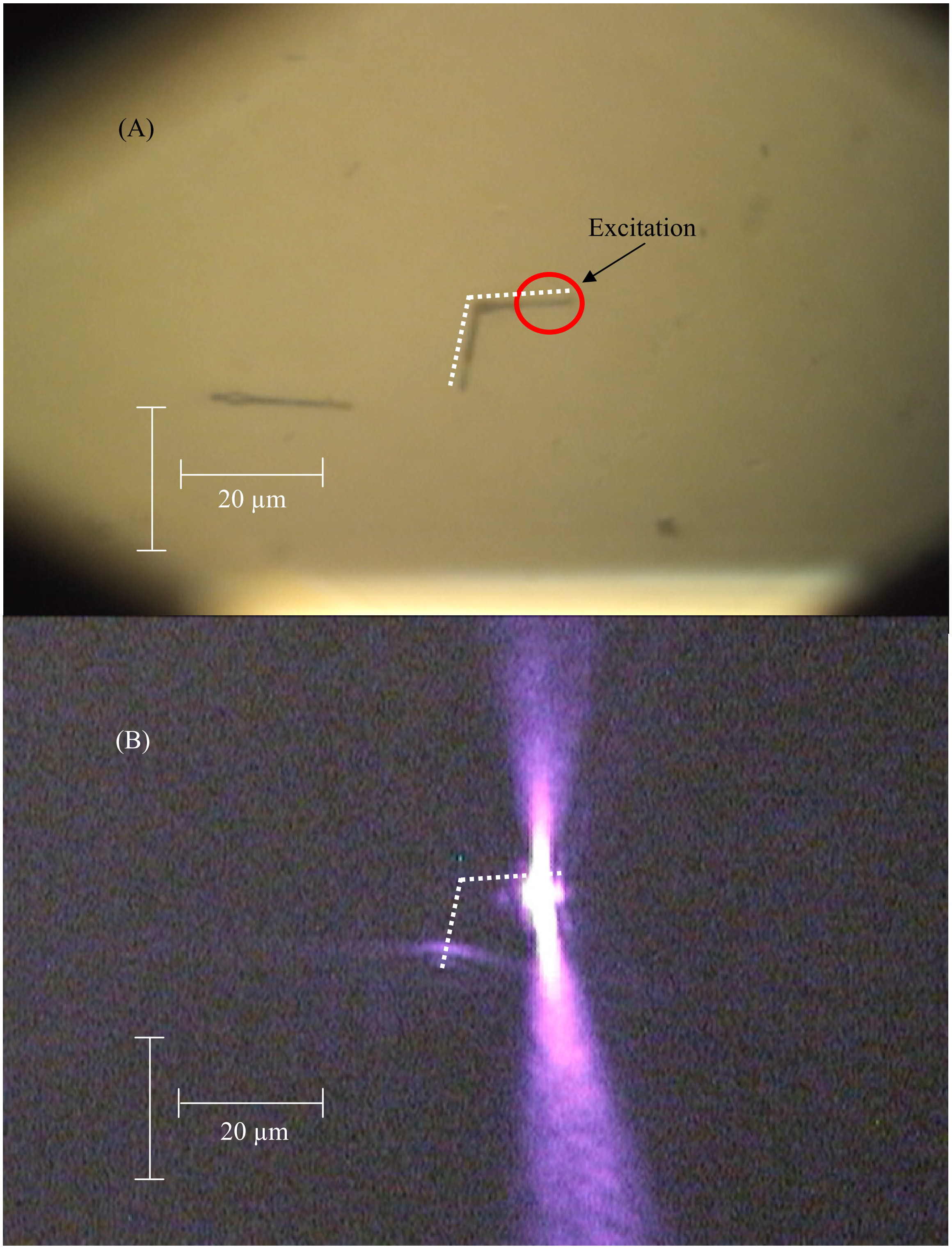

Figure 25: Excitation (A) and scatter (B) from a partial tetrapod.

5.2 Photoluminescence

While attempting to view the propagation of light through the structures, a result involving blue-green photoluminescence was observed while attempting to use an older tetrapod sample to view light propagation through the tetrapod structure. The blue-green photoluminescence seen from the ZnO structures seemed to be stronger from these older structures and showed some unusual characteristics. When a perfectly vertically aligned leg was excited the blue-green photoluminescence was concentrated in spherical defects in the center of the structure as seen in Figure 26.

If a leg that was not perfectly vertical was excited, the photoluminescence was seen along the entire length of the excited area as seen in Figure 27. The presence of the strong blue-green photoluminescence in these structures was probably caused by the sample reacting with oxygen from the atmosphere as it aged, increasing the number of oxygen defects generally cited for this type of photoluminescence.[3] The photoluminescence seemed to be excited by the second harmonic radiation. The appearance of the light concentrating at one location in Figure 26 may have been a case of the second harmonic bleaching out the other radiation as it was much stronger in that configuration, but could also have a more interesting explanation such as lasing, but this is not likely.

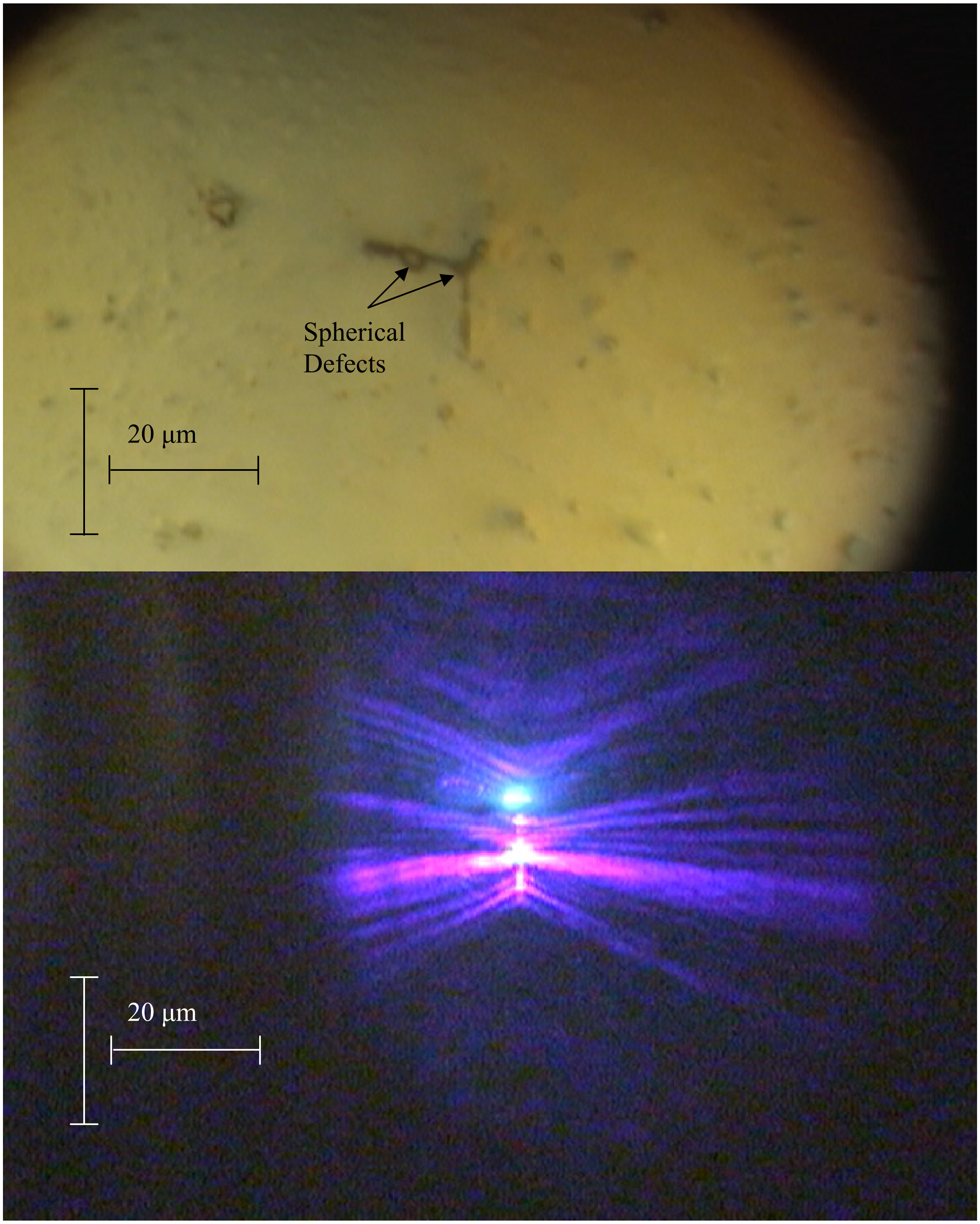

Figure 26: Photoluminescence from the vertical leg of a tetrapod.

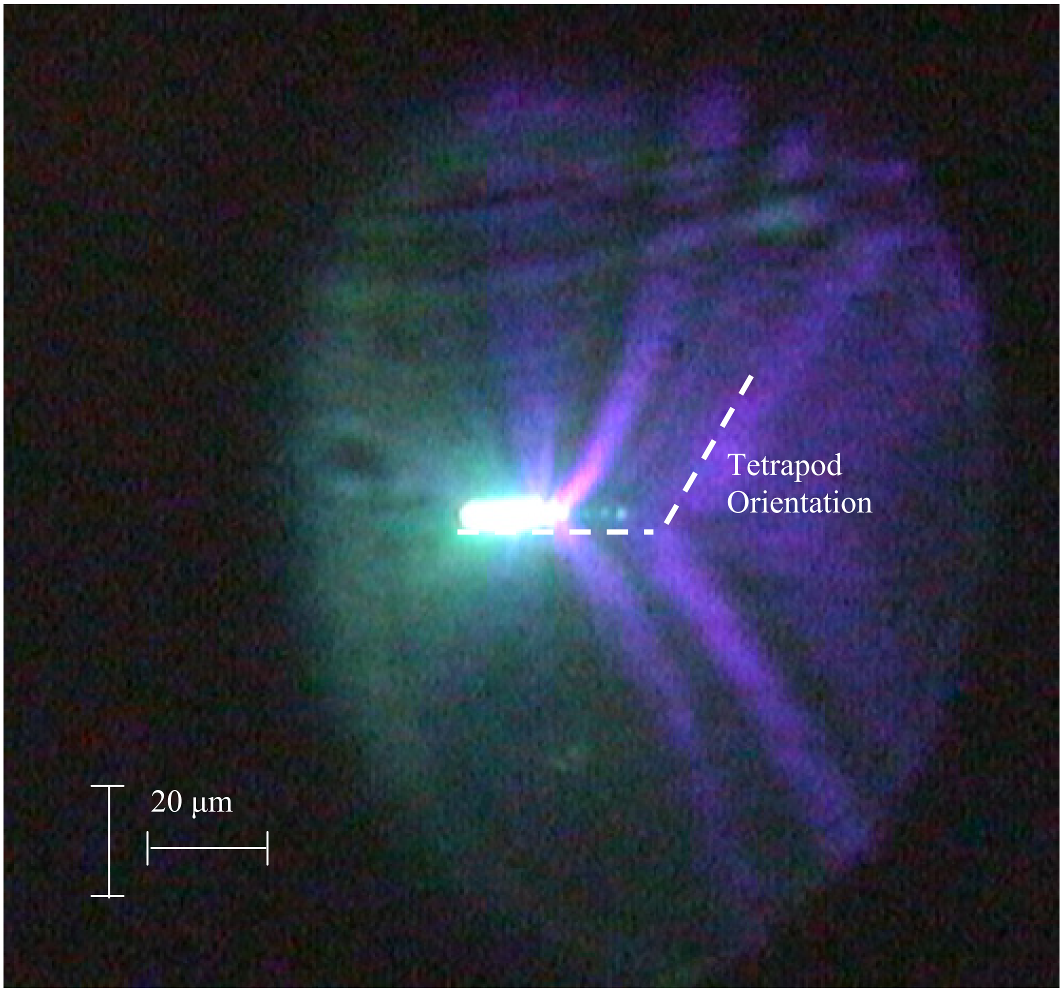

Figure 27: Photoluminescence from the horizontal leg of a partial tetrapod.

Chapter 6: Conclusions

In this thesis a method was presented for determining the nonlinear coefficients of the second order susceptibility tensor for ZnO nanorods. The method avoided many of the drawbacks of previously used techniques and could easily be use on other types of materials.

Models were created to describe the second harmonic scattering patterns of both a structure of two rods joined at an angle of 120º and a tetrapod. The model of the two joined rods seemed to accurately predict the shape and number of fringes in the second harmonic scatter pattern as seen from the prediction of leg length as mentioned in Section 4.1, while the tetrapod model only had a faint resemblance to the experimental scatter pattern. Future work on this model might include an accounting for the fourth leg of the tetrapod. Both models would benefit from a more accurate knowledge of the structure's orientation.

Finally, propagation of second harmonic radiation through a partial ZnO tetrapod was observed. More experimentation is required on this subject in order to determine with certainty that it propagation, and not absorption and re-emissions that are being observed as well as determining whether it is the fundamental or second harmonic radiation that is propagating. More experimentation on with the photoluminescence in older structures might also provide useful information. The concentration of photoluminescence with the higher levels of excitation might prove to be an important characteristic.

References

1. Z.L. Wang, Materials Today **7,** 26 (2004).
2. A.B. Djurišić, Y.H. Leung, Small, **2**, 944 (2006).
3. Ozgur et al., Journal of Applied Physics **98**, 041301 (2005).
4. Könenkamp et al., Applied Physics Letters **85**, 6004 (2004).
5. Hauschild et al., Phys. Stat. Sol. C **3**, No. 7, 2514–2517 (2006).
6. Hauschild et al., Phys. Stat. Sol. C **3**, No. 10, 3557–3560 (2006).
7. Sun et al., Phys. Rev. Lett. **100,** 156403 (2008).
8. Johnson et al., J. Phys. Chem. B **105** No. 46 (2001).
9. Mondia et al., Applied Physics Letters **93**, 121102 (2008).
10. Johnson et al., J. Phys. Chem. B **107**, 8816 (2003).
11. Zhang et al., Applied Physics Letters **90**, 153116 (2007).
12. Song et al., J. Phys. Chem. B **109***,* 15749 (2005).
13. Kachynsky et al., J. Phys. Chem. C **112**, 10721 (2008).
14. A. Yariv, P. Yeh, *Photonics: Optical Electronics in Modern Communications* 6th Ed. (Oxford University Press, New York, 2007).
15. P.J. Campagnola, L.M. Loew, Nature Biotechnology vol 21, no 11, 1356 (2003).
16. Dadap, Phys. Rev. B **78** (2008).
17. Johnson et al., Nano Letters **2** No. 4, 279 (2002).
18. Liu et al., Optics Express vol **15**, no **17**, 10666 (2007).
19. Long et al., Nano Letters vol **7**, no **3** (2007).
20. Liu et al., Phys Rev B **77** (2008).
21. Geren et al., Journal of Applied Physics, accepted for publication.
22. Zhang et al., Journal of the American Chemical Society vol. 128, no 33 (2006).
23. J. E. Sipe, J. Opt. Soc. Am. B **4**, 481 (1987).

24. Sipe et al., Phys. Rev. B **35**, 1129 (1987).

25. R.C. Miller, W.A. Nordland, Appl. Phys. Lett. **16**, 4, 174 (1970).

26. R.C. Weast, *CRC: Handbook of Chemistry and Physics 67th ed.* (CRC Press, Inc. 1986).

27. J.D. Jackson, Classical Electrodynamics (Wiley, New York, 1999).

Appendix A: Matlab code used to simulate the a single dipole.

```
%Vector simulation of dipole
clear                               % clears all variables
deff=18e-6;                         % set effective distance
L=1.5e-6;                           % set length of dipoles
dy1=L/138;                          % set discretization along length of dipole
lambda=810e-9;                      % set fundamental wavelength
c=2.998e8;                          % define speed of light
pi=3.14159;
k=2*pi/lambda;                      % define k-vector
eps=8.854e-12;                      % define epsilon

y=-40:0.4:40;                       % set y-dimension of the viewing window
y=y*1e-6;

x=-41:0.4:41;                       % set x-dimension of the viewing window
x=x*1e-6;

y1=0:dy1:L;                         % variable for position on the dipole
half=int32(size(y1,2)/2);           % location of the twinning plane
TotalSteps=size(x,2)                % used for monitoring simulation time


for xs=1:size(x,2)                  % integrate over x-direction
   timeStep=xs                      % used for monitoring simulation time
   for ys=1:size(y,2)               % integrate over y-direction

      intE=0;                       % zeroing integrals
      intH=0;

      for y1s=1:half                % integrate over length of dipole
         y1s2=y1s+half-1;           % variable for second half of dipole
         final=[x(xs) y(ys) deff];  % point in viewing plane
         initial=[0 y1(y1s) 0];     % point on dipole
         initial12=[0 y1(y1s2) 0];  % points on second half of dipole

         n=(final-initial);         % unit vectors from  dipole to viewing plane
         n=n./sqrt(n(1)^2+n(2)^2+n(3)^2);

         n12=(final-initial12);
                       % unit vectors from second half of dipole to viewing plane
         n12=n12./sqrt(n12(1)^2+n12(2)^2+n12(3)^2);
```

```
      p=L^2/2.*[0 1 -0.50];           % dipole moment

      p12=-L^2/2.*[0 1 -0.50];        % dipole moment from opposite dipole

      % distances from point on dipole to point in viewing plane
      r1=((x(xs)-initial(1))^2+(y(ys)-initial(2))^2+(deff-initial(3))^2)^(1/2);

      r12=((x(xs)-initial12(1))^2+(y(ys)-initial12(2))^2+(deff-
           initial12(3))^2)^(1/2);

      % Calculating the fields caused by the current point on each dipole
      H1=c*k^2/(4*pi).*cross(n,p).*exp(2i*k*r1)/r1.*(1-1./(2i*k*r1));
      E1=k^2.*cross(cross(n,p),n).*exp(2i*k*r1)./r1;
      E1=E1+(3.*n.*dot(n,p)-p).*(1/r1^3-1i*k/r1^2).*exp(2i*r1*k);
      E1=1/(4*pi*eps).*E1;


      H12=c*k^2/(4*pi).*cross(n12,p12).*exp(2i*k*r12)/r12.*(1-
           1./(2i*k*r12));
      E12=k^2.*cross(cross(n12,p12),n12).*exp(2i*k*r12)./r12;
      E12=E12+(3.*n12.*dot(n12,p12)-p12).*(1/r12^3-
           1i*k/r12^2).*exp(2i*r12*k);
      E12=1/(4*pi*eps).*E12;


      % removing the z-directed component (direction of propagation)
      E1(3)=0;
      H1(3)=0;

      E12(3)=0;
      H12(3)=0;


      %Calculation the running field integrals
      intE=intE+E1.*dy1+E12.*dy1;
     intH=intH+H1.*dy1+ H12.*dy1;

    end

    % calculate Poynting vector for view point
    s=abs(cross(intE,conj(intH)));
    S(xs,ys)=sqrt(s(1)^2+s(2)^2+s(3)^2);

  end
end
```

```
surf(y,x,abs(S));                    % plot Poynting vector in view plane
```

Appendix B: Matlab code used to simulate the three-dimensional twinned tetrapod structure

```
%Vector simulation of tetrapod
clear                              % clears all variables
deff=120e-6;                       % set effective distance
L=7.9e-6;                          % set length of dipoles
dy1=L/138;                         % set discretization along length of dipole
lambda=810e-9;                     % set fundamental wavelength
c=2.998e8;                         % define speed of light
pi=3.14159;
k=2*pi/lambda;                     % define k-vector
eps=8.854e-12;                     % define epsilon

y=-80:0.8:80;                      % set y-dimension of the viewing window
y=y*1e-6;

x=-81:0.8:81;                      % set x-dimension of the viewing window
x=x*1e-6;

y1=0:dy1:L;                        % variable for position on the dipole
half=int32(size(y1,2)/2);          % location of the twinning plane
TotalSteps=size(x,2)               % used for monitoring simulation time


for xs=1:size(x,2)                 % integrate over x-direction
  timeStep=xs                      % used for monitoring simulation time
  for ys=1:size(y,2)               % integrate over y-direction

    intE=0;                        % zeroing integrals
    intH=0;

    for y1s=1:half                 % integrate over length of dipole
      y1s2=y1s+half-1;             % variable for second half of dipole
      final=[x(xs) y(ys) deff];    % point in viewing plane
      initial=[0 y1(y1s) -0.5];            % point on first dipole
      initial2=y1(y1s).*[0.866025 -0.5 -0.5];        % point on second dipole
      initial3=y1(y1s).*[-0.866025 -0.5 -0.5];       % point on third dipole

                                   % points on second half of dipoles
      initial12=[0 y1(y1s2) -0.5];
      initial22=y1(y1s2).*[0.866025 -0.5 -0.5];
      initial32=y1(y1s2).*[-0.866025 -0.5 -0.5];
```

```
n=(final-initial);              % unit vectors from  dipole to viewing plane
n2=(final-initial2);
n3=(final-initial3);
n=n./sqrt(n(1)^2+n(2)^2+n(3)^2);
n2=n2./sqrt(n2(1)^2+n2(2)^2+n2(3)^2);
n3=n3./sqrt(n3(1)^2+n3(2)^2+n3(3)^2);
                                % unit vectors from second half of dipole to
                                   viewing plane
n12=(final-initial12);
n22=(final-initial22);
n32=(final-initial32);
n12=n12./sqrt(n12(1)^2+n12(2)^2+n12(3)^2);
n22=n22./sqrt(n22(1)^2+n22(2)^2+n22(3)^2);
n32=n32./sqrt(n32(1)^2+n32(2)^2+n32(3)^2);

p=L^2/2.*[0 1 -0.50];           % dipole moments
p2=L^2/2.*[0.866025 -0.5 -0.5];
p3=L^2/2.*[-0.866025 -0.5 -0.5];

p12=-L^2/2.*[0 1 -0.50];        % dipole moments from opposite dipole
p22=-L^2/2.*[0.866025 -0.5 -0.5];
p32=-L^2/2.*[-0.866025 -0.5 -0.5];

% distances from point on dipole to point in viewing plane
r1=((x(xs)-initial(1))^2+(y(ys)-initial(2))^2+(deff-initial(3))^2)^(1/2);
r2=((x(xs)-initial2(1))^2+(y(ys)-initial2(2))^2+(deff-initial2(3))^2)^(1/2);
r3=((x(xs)-initial3(1))^2+(y(ys)-initial3(2))^2+(deff-initial3(3))^2)^(1/2);

r12=((x(xs)-initial12(1))^2+(y(ys)-initial12(2))^2+(deff-
     initial12(3))^2)^(1/2);
r22=((x(xs)-initial22(1))^2+(y(ys)-initial22(2))^2+(deff-
     initial22(3))^2)^(1/2);
r32=((x(xs)-initial32(1))^2+(y(ys)-initial32(2))^2+(deff-
     initial32(3))^2)^(1/2);

% Calculating the fields caused by the current point on each dipole
H1=c*k^2/(4*pi).*cross(n,p).*exp(2i*k*r1)/r1.*(1-1./(2i*k*r1));
E1=k^2.*cross(cross(n,p),n).*exp(2i*k*r1)./r1;
E1=E1+(3.*n.*dot(n,p)-p).*(1/r1^3-1i*k/r1^2).*exp(2i*r1*k);
E1=1/(4*pi*eps).*E1;

H2=c*k^2/(4*pi).*cross(n2,p2).*exp(2i*k*r2)/r2.*(1-1./(2i*k*r2));
E2=k^2.*cross(cross(n2,p2),n2).*exp(2i*k*r2)./r2;
E2=E2+(3.*n2.*dot(n2,p2)-p2).*(1/r2^3-1i*k/r2^2).*exp(2i*r2*k);
E2=1/(4*pi*eps).*E2;
```

```
H3=c*k^2/(4*pi).*cross(n3,p3).*exp(2i*k*r3)/r3.*(1-1./(2i*k*r3));
E3=k^2.*cross(cross(n3,p3),n3).*exp(2i*k*r3)./r3;
E3=E3+(3.*n3.*dot(n3,p3)-p3).*(1/r3^3-1i*k/r3^2).*exp(2i*r3*k);
E3=1/(4*pi*eps).*E3;

H12=c*k^2/(4*pi).*cross(n12,p12).*exp(2i*k*r12)/r12.*(1-
      1./(2i*k*r12));
E12=k^2.*cross(cross(n12,p12),n12).*exp(2i*k*r12)./r12;
E12=E12+(3.*n12.*dot(n12,p12)-p12).*(1/r12^3-
      1i*k/r12^2).*exp(2i*r12*k);
E12=1/(4*pi*eps).*E12;

H22=c*k^2/(4*pi).*cross(n22,p22).*exp(2i*k*r22)/r22.*(1-
      1./(2i*k*r22));
E22=k^2.*cross(cross(n22,p22),n22).*exp(2i*k*r22)./r22;
E22=E22+(3.*n22.*dot(n22,p22)-p22).*(1/r22^3-
      1i*k/r22^2).*exp(2i*r22*k);
E22=1/(4*pi*eps).*E22;

H32=c*k^2/(4*pi).*cross(n32,p32).*exp(2i*k*r32)/r32.*(1-
      1./(2i*k*r32));
E32=k^2.*cross(cross(n32,p32),n32).*exp(2i*k*r32)./r32;
E32=E32+(3.*n32.*dot(n32,p32)-p32).*(1/r32^3-
      1i*k/r32^2).*exp(2i*r32*k);
E32=1/(4*pi*eps).*E32;

% removing the z-directed component (direction of propagation)
E1(3)=0;
H1(3)=0;
E2(3)=0;
H2(3)=0;
E3(3)=0;
H3(3)=0;

E12(3)=0;
H12(3)=0;
E22(3)=0;
H22(3)=0;
E32(3)=0;
H32(3)=0;


%Calculation the running field integrals
intE=intE+E1.*dy1.*3^2+E2.*dy1.*1.9147^2+E3.*dy1.*1.9147^2+E12.*
      dy1.*3^2+E22.*dy1.*1.9147^2+E32.*dy1.*1.9147^2;
```

```
        intH=intH+H1.*dy1+H2.*dy1+H3.*dy1+H12.*dy1+H22.*dy1+H32.*dy1;

      end

      % calculate Poynting vector for view point
      s=abs(cross(intE,conj(intH)));
      S(xs,ys)=sqrt(s(1)^2+s(2)^2+s(3)^2);

   end
end

surf(y,x,abs(S));                    % plot Poynting vector in view plane
```

Appendix C: Description of Research for Popular Publication

PATTERNS IN LIGHT

Second harmonic imaging of micro- and nanostructures

BY KATRINA GEREN

With the continuing decrease in the size of devices, the size of optical components of the devices must also decrease. In order to effectively incorporate these small components, their characteristics must be accurately understood. This leads to an area of study that is nothing if not pretty.

Recently, scientists such as Dr. Min Xiao and his graduate student Katrina Geren (otherwise known as the author) have been pursuing investigation of the second harmonic characteristics of micro- and nanosized crystals. Second harmonic characteristics of a crystal involve its ability to convert light to double its original frequency. Basically, when you hit a certain type of crystal with a focused laser beam it will convert some of the light to a wavelength half as large as the original (and twice the frequency). Much of the investigation of this property has centered upon Zinc Oxide structures due to their current popularity as a basis for nanodevices. It has been said that "ZnO could be one of the most Important nanomaterials in future research and applications."[1] Further understanding of the optical properties of the structures will increase the possibilities for their use in tiny devices such as lasers, frequency doublers, and second harmonic bioprobes. This is where the research into the second harmonic characteristics becomes important.

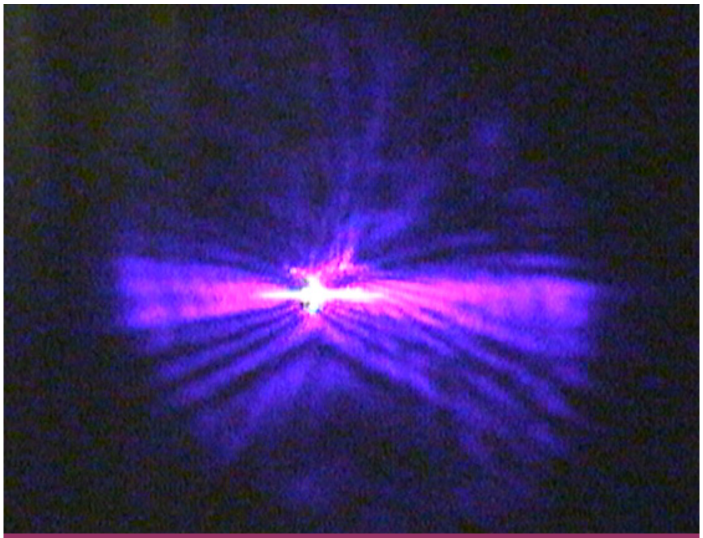

INTENSITY PATTERNS -- The bright sections in the center of the image are the three visible legs of a tetrapod. Tetrapods are of particular interest due to their popularity for use as nanolasers.

At the University of Arkansas Dr. Xiao and his research group have been studying the intensity patterns of the second harmonic radiation from these ZnO nano- and microstructures, as well as the second order susceptibility of the structures that governs this type of radiation. This is accomplished by illuminating the structures with a near infrared laser beam and observing the results with a digital camcorder. Studies of the resulting images of the second harmonic intensity patterns of ZnO nanorods have revealed a dipole like pattern from the structures as detailed in the March 2008 Physics Review B.[2] Basically, the rods are giving off second harmonic radiation in patterns that closely parallel the radiation patterns of standard dipole antennas. This has led to the question of whether more complex structures will also display this dipole like behavior.

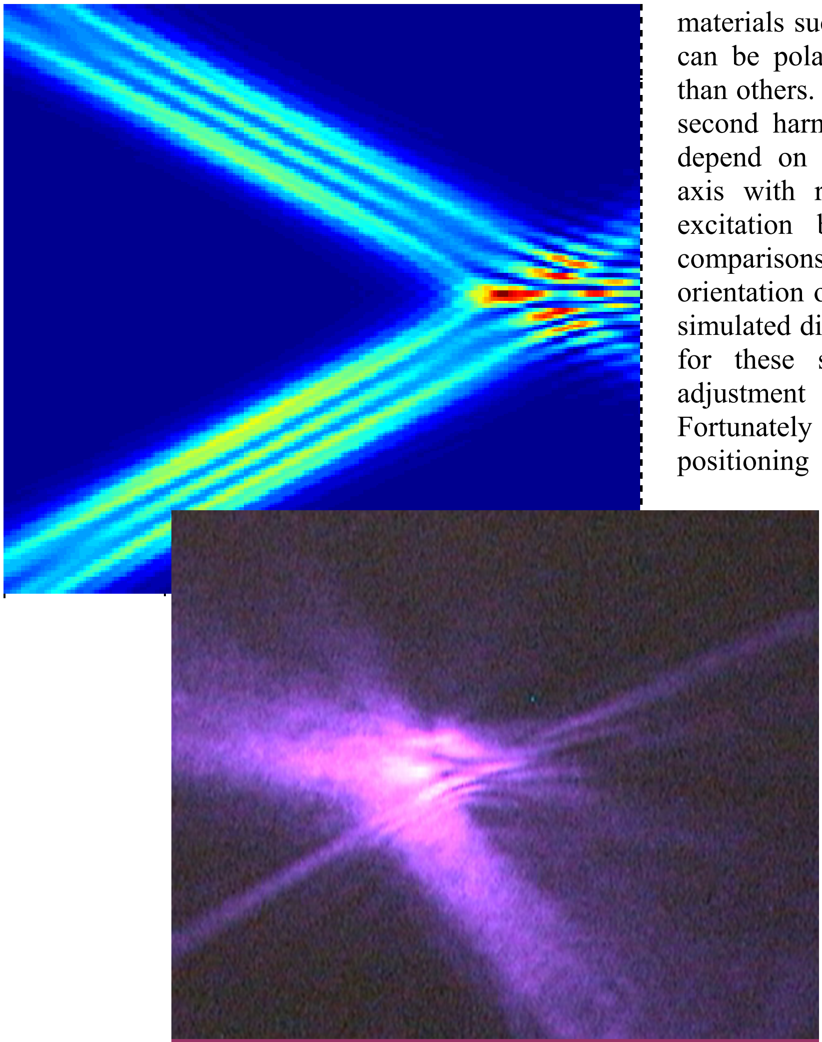

ROUGH COMPARISONS -- A comparison between a simulated (blue background) and experimental (black background) intensity pattern for a structure made up of two legs shows a rough match.

Initial images on this subject indicate that this is likely, but matches between various more complex crystalline nanostructures and simulations of dipole structures have not been as close as those made between single dipoles and nanorods. The elements of the basic patterns are the same, but the weighting of the individual elements seems to vary between the two. The addition of a component in the simulation to account for the directionality of the susceptibility which determines the intensity of the second harmonic radiation accounted for some of this difference, though the location of the pattern is still slightly off. The lack of symmetry in noncentrosymmetric crystalline materials such as ZnO means that the structures can be polarized more easily in one direction than others. This means that the intensity of the second harmonic radiation from the structures depend on the orientation of their crystalline axis with respect to the polarization of the excitation beam. The difficulty with these comparisons is that of exactly matching the orientation of the test structures with that of the simulated dipoles. The test setup currently used for these studies does not allow for fine adjustment of the structure's orientation. Fortunately work is being done elsewhere on a positioning mechanism for the purpose of studying tetrapod lasers.[3]

Difficulty also arises from the idea that to observe something is to change it. Apparently, this is especially true when one is observing nanostructures with a laser beam of reasonably high intensity such as that needed to observe clear second harmonic patterns. In this case, the structures do not always survive the observation. This makes retesting structures difficult on occasion (especially if the researcher does not realized that the sample is being destroyed at the time). Even if the structures are not completely obliterated, if one is not careful, they can be damaged by the excitation laser. This makes reproducing results difficult as well. As a high intensity is needed to create the phenomenon, this problem is unlikely to be solved, so it must be managed by thoughtful laser management. Intensity attenuators are also helpful.

In addition to understanding the second harmonic radiation patterns of different structures, knowledge of the method of light propagation through a structure is also important. In order to put multiple devices together to perform a function such as optical repeating, the light must couple between the devices. In order to successfully string devices together you must know how the light moves through your device. Propagation through a microstructure has been tentatively seen by illuminating only one leg of a multi-branch structure and observing the other legs. Unfortunately, the data does not conclusively prove that the second harmonic radiation and not the original beam is what was observed. This will require more research.

It has been written that "ZnO is probably the richest family of nanostructures among all one-dimensional nanostructures, including carbon nanotubes."[1] But in order to morph these structures into useful devices their characteristics must be determined and in order for these devices to be integrated into functional systems the way the light moves through the structures must also be known. That is why this research is important.

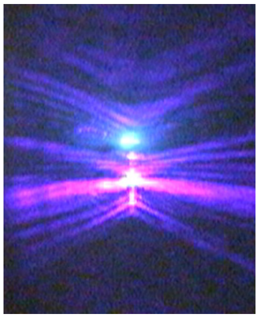

---

1. Z.L. Wang, Materials Today (June 2004)
2. Lui et al, Physics Review B **77** (2008)
3. Mondia et al, Physics Letters **93** (2008)

Appendix D: Executive Summary of Newly Created Intellectual Property

The following list of new intellectual property items were created in the course of this research project and should be considered from both a patent and commercialization perspective.

1. A method for determining the nonlinear coefficients of susceptibility of single nanorods.
2. A model of two joined ZnO nanorods, programmed in the matlab environment.
3. A model of a ZnO tetrapod, programmed in the Matlab environment.

Appendix E: Potential Patent and Commercialization Aspects of listed Intellectual Property Items

E.1 Patentability of Intellectual Property

The three items listed were considered first from the perspective of whether or not the item could be patented.

1. The new method for determining the second order susceptibility coefficients can probably be patented. It is very close to previously published techniques for thin films though, so there might be some difficulty in the patent process.
2. The model for the two joined ZnO rods can probably be patented. Difficulty might arise as it is a fairly obvious approach and a similar approach was published in *Physics Review* B **77**.
3. The model for the ZnO tetrapod can probably be patented. Difficulty might arise as it is a fairly obvious approach and a similar approach was published in *Physics Review* B **77**.

E.2 Commercialization Prospects

The three items listed were then considered from the perspective of whether or not the item should be patented.

1. The method for determining the second order susceptibility coefficients should not be patented as it is not expected to provide significant commercial value because once the data I known finding it again would not be necessary and because the patent could be easily bypassed.

2. The model of two joined ZnO rods should not be patented as it is not expected to provide significant commercial value because it was not developed enough to be suitable in this form for practical applications.
3. The model of the ZnO tetrapod should not be patented as it is not expected to provide significant commercial value because it is not accurate enough to be suitable for practical applications

E.3 Possible Prior Disclosure of IP

The following items were discussed in a public forum or have published information that could impact the patentability of the listed IP.

1. The method for determining the second order susceptibility coefficients has been accepted to be published in the Journal of Applied Physics under the title "Second-order Susceptibilities of ZnO Nanorods from Forward Second-harmonic Scattering."
2. The model of the two joined ZnO rods has been presented in the closed Microelectronics-Photonics Research Communications seminar for students in the Microelectronics-Photonics Graduate Program.
3. The model of the ZnO tetrapod has been presented in the closed Microelectronics-Photonics Research Communications seminar for students in the Microelectronics-Photonics Graduate Program.

Appendix F: Broader Impact of Research

F.1 Applicability of Research Methods to Other Problems

The research methods presented above are highly applicable to other problems. The method for determining nonlinear coefficients could be applied to many different types of material, though the calculations would have to be redone for different crystal symmetry classes.

The modeling approach used for the two joined rods and the tetrapod have already been successfully applied to other types of material and structures. The dipole moment just has to be altered to point in the direction of the polarity of the crystal.

F.2 Impact of Research Results on U.S. and Global Society

The research should have little or no effect on U.S. and Global Society because as of yet, this is not applied research.

F.3 Impact of Research Results on the Environment

The research results should have no effect on the environment as they are simply another way to observe material properties using standard equipment.

Appendix G: Microsoft Project for MS MicroEP Degree Plan

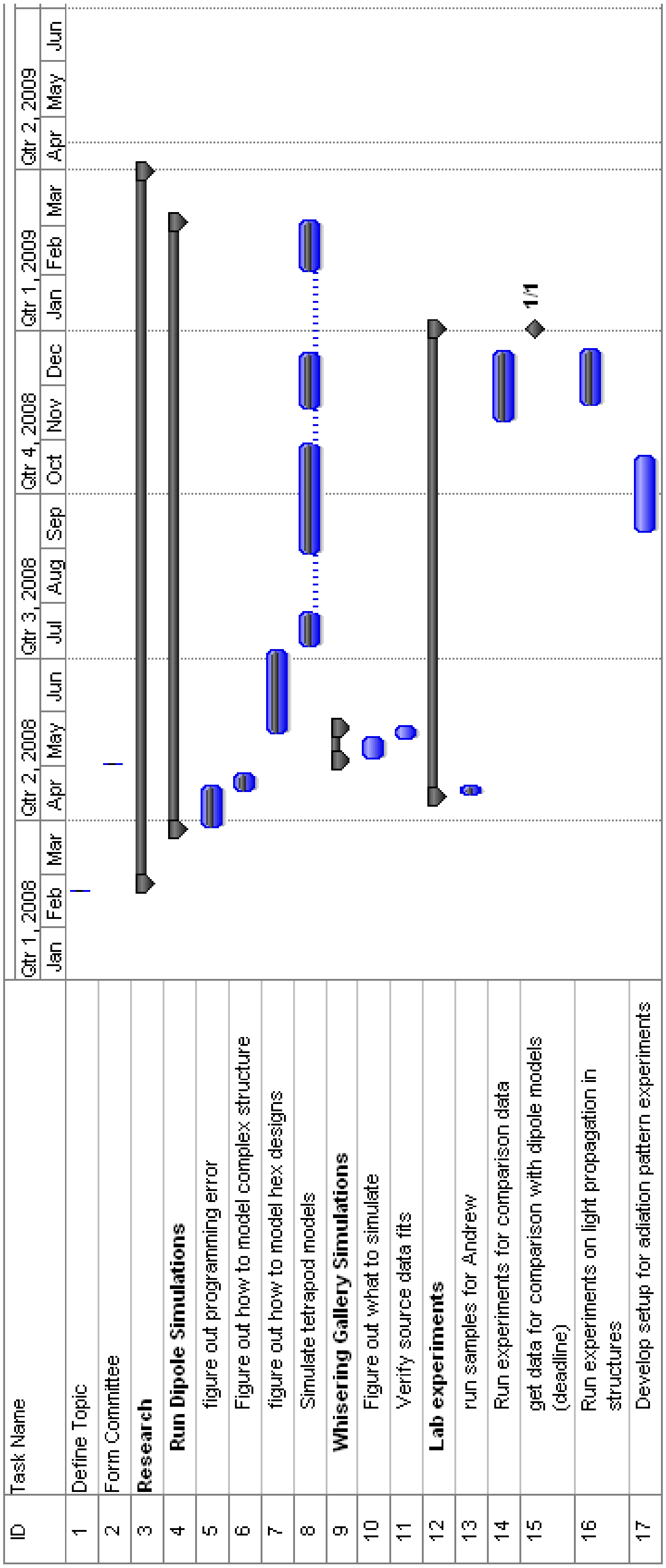

ID	Task Name
1	Define Topic
2	Form Committee
3	**Research**
4	**Run Dipole Simulations**
5	figure out programming error
6	Figure out how to model complex structure
7	figure out how to model hex designs
8	Simulate tetrapod models
9	**Whisering Gallery Simulations**
10	Figure out what to simulate
11	Verify source data fits
12	**Lab experiments**
13	run samples for Andrew
14	Run experiments for comparison data
15	get data for comparison with dipole models (deadline)
16	Run experiments on light propagation in structures
17	Develop setup for adiation pattern experiments

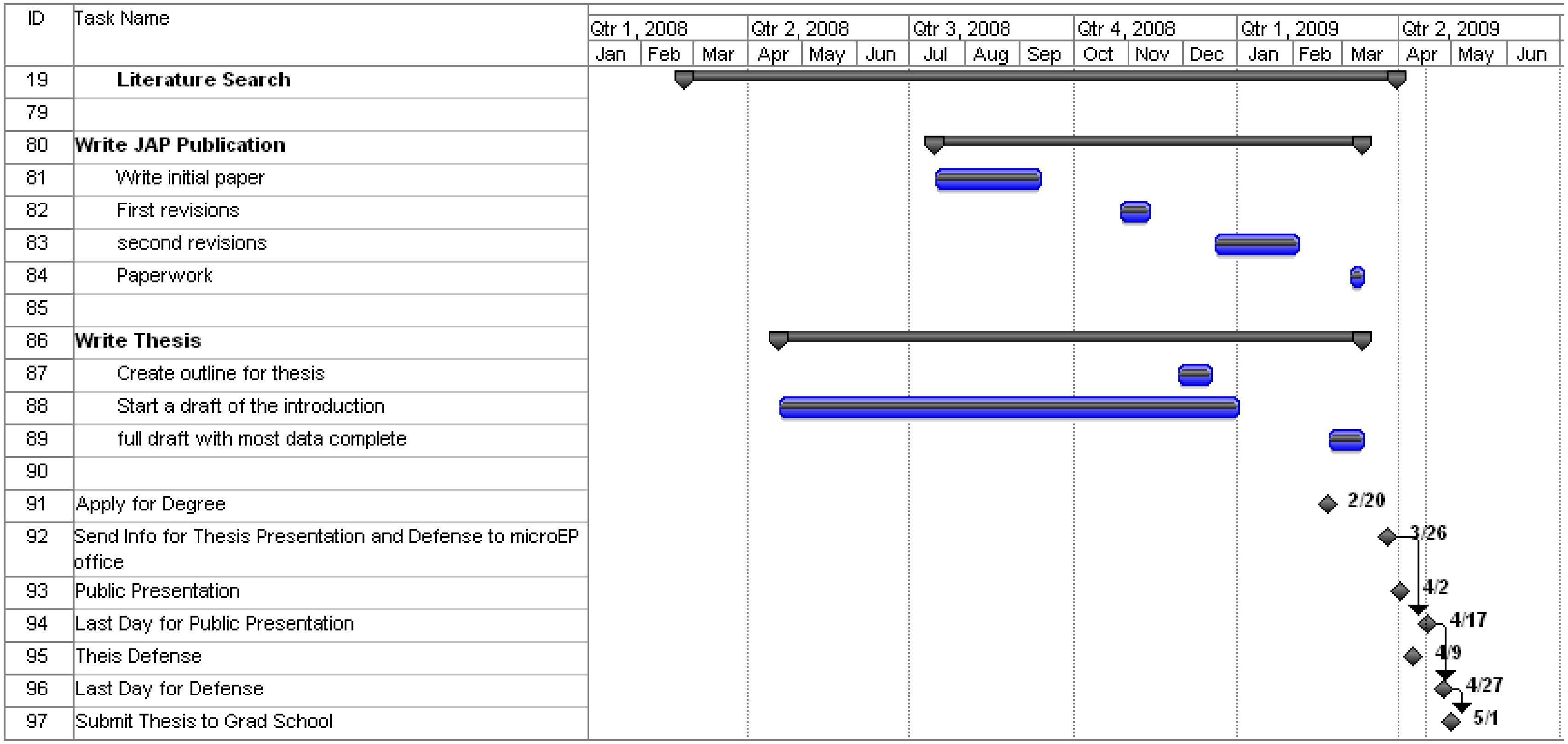

ID	Task Name
19	**Literature Search**
79	
80	**Write JAP Publication**
81	Write initial paper
82	First revisions
83	second revisions
84	Paperwork
85	
86	**Write Thesis**
87	Create outline for thesis
88	Start a draft of the introduction
89	full draft with most data complete
90	
91	Apply for Degree
92	Send Info for Thesis Presentation and Defense to microEP office
93	Public Presentation
94	Last Day for Public Presentation
95	Theis Defense
96	Last Day for Defense
97	Submit Thesis to Grad School

Appendix H: Identification of All Software Used in Research and Thesis Generation

Computer #1:
- Model Number: Dell Intel(R)
- Serial Number: 0045-438-792-640
- Location: PHYS248
- Owner: Fulbright College

Software #1:
- Name: Microsoft Office 2007
- Purchased by: UA Physics Dept.

Computer #2:
- Model Number: Dell Optiplex GX620
- Serial Number: 76487-OEM-0011903-00102
- Location: CHEM 325
- Owner: Fulbright College

Software #1:
- Name: Microsoft Office 2003
- Purchased by: Lois Geren (University of Arkansas)

Software #2:
- Name: Adobe Acrobat 8.0 Professional
- Purchased by: Fulbright College

Computer #3
- Model Number: Gateway e-series
- Serial Number: 0027784071
- Location: 16116 Pin Oak rd, Fayetteville, AR
- Owner: Katrina Geren

Software #1:
- Name: MATLAB 7 SV
- Purchased by: Katrina Geren

(signature of student)	(signature of major professor)
____________________________	____________________________
Katrina Geren	Dr. Min Xiao

Filename: ThesisDraftB5[2]
Directory: C:\Users\lgeren\Documents
Template: C:\Users\lgeren\AppData\Roaming\Microsoft\Templates\Normal.dotm
Title: 1
Subject:
Author: Katrina Geren
Keywords:
Comments:
Creation Date: 4/8/2009 10:32:00 AM
Change Number: 63
Last Saved On: 4/23/2009 11:21:00 PM
Last Saved By: lgeren
Total Editing Time: 978 Minutes
Last Printed On: 4/23/2009 11:21:00 PM
As of Last Complete Printing
  Number of Pages: 83
  Number of Words: 12,812 (approx.)
  Number of Characters: 73,031 (approx.)